Probing statistical properties of Ni, Ge, Nd and Sm isotopes

Therese Renstrøm

Thesis submitted in partial fulfilment of the requirements for the degree of philosophiae doctor

Department of Physics
Faculty of Mathematics and Natural Sciences
University of Oslo

August 2015

Series of dissertations submitted to the
Faculty of Mathematics and Natural Sciences, University of Oslo
No. 1680

ISSN 1501-7710

Cover: Hanne Baadsgaard Utigard.
Print production: John Grieg AS, Bergen.

Produced in co-operation with Akademika Publishing.
The thesis is produced by Akademika Publishing merely in connection with the thesis defence. Kindly direct all inquiries regarding the thesis to the copyright holder or the unit which grants the doctorate.

Acknowledgments

First of all I would like to express my gratitude to my supervisors. Thank you Sunniva Siem for giving me the opportunity to be a part of your research group, for always being so encouraging and kind and letting me take part in many interesting experiments all over the world. To Ann-Cecilie Larsen, thank you for your careful reading of and feedback on this thesis, and for inspiring scientific conversations. I would also like to thank Magne Guttormsen for kindly giving excellent feedback on to all scientific questions. Your enthusiasm for data analysis is contagious.

A big thanks to Hiroaki Utsunomiya for letting me join the *KOBe*$^{-}$ collaboration, and including me in the NewSUBARU experiments. A thanks to the *Bucharest team* (Dan & Ioana), it has been a pleasure to work with you!

Also, I am very grateful to Ronald Schwengner and Alex Brown for providing me with excellent shell-model calculations. A special thanks to Ronald for allowing me to show his unpublished results from the Ge-campaign.

To my friends and colleagues at work. Thank you for making the nuclear physics group a warm and interesting working place, and for all the support. A special "teşekkürler" to Eda (for "babysitting" in the late hours writing), "gracias" to Frank and Victor and "dzięki" to Kasia for great fun, trips and dinners, and for all the help. Thank you Gry, my ex-officepartner, for reading this thesis and giving excellent feedback.

To Hilde. I have enjoyed your company enormously, both at the office and at experiments. Thank you for being so kind, funny and smart.

To Christian, thanks for providing valuable comments to the thesis. You are absolutely brilliant.

To my dear flat mates, Ester, Kristine and Ane, thank you for your kindness and craziness.

Thank you Maren, Anne-Lene and Siv, my lovely companions in adventures on the bike and in the climbing wall.

To Gro Elise, you are both beautiful and an excellent proofreader :-) Thank you for all your help this stressful summer.

Last but not least, I would like to thank my family. You are the best! Margrethe, Renate, Reidun and Harald! I love you. Without your love and care I would not have been able to do this. You have helped me in every way possible.

Therese Renstrøm

August, 2015

Contents

Chapter 1

Introduction

We are all in the gutter, but some of us are looking at the stars
OSCAR WILDE (1854-1900)

This introduction consists of a historical background of basic nuclear physics, with focus on important developments, many of which had astrophysical implications. A brief introduction to stellar nucleosynthesis processes and important nuclear physics input in these processes will also be given. The aim of this chapter is to provide a context to the experiments performed within the scope of this thesis, as well as to further illuminate the scientific motivations behind this work.

1.1 A short history of nuclear astrophysics

The nuclear atom, introduced by Ernest Rutherford in the late spring of 1911, consists of a massive, positive charge at its centre surrounded by a sphere of opposite charge. Rutherford pictured the nucleus as a highly complex body. In his own words: "No doubt the positively charged centre of the atom is a complicated system in movement" [1]. But the nuclear model was first met with indifference and not considered as a theory of the constitution of the atom, until Niels Bohr in 1913 turned Rutherford's picture into a proper quantum atomic theory. Shortly after, several physicists started speculating about the structure of the complex and tiny nucleus.

In 1914 Rutherford commented:"The general evidence indicates that the primary β-particles arise from a disturbance of the nucleus. The latter must consequently be considered as a very complex structure consisting of positive particles and electrons, but it is premature to discuss at the present time the possible structure of the nucleus itself" [2]. From this point on the general view was that the

nucleus was the origin of all radioactivity and was made up of electrons and positive particles, the latter given the name protons by Rutherford in 1920.

Due to the almost complete lack of experimental evidence, constructing reliable nuclear models proved a hopeless task. In his Bakerian lecture in 1920, Rutherford suggested that particles other than electrons, αs, and protons might exist; for example a neutral particle made up of one electron and one proton, a "neutron". Rutherford immediately assigned some of his students the task of searching for the proposed neutral object. Attempts to detect the hypothetical particle were made on several occasions during the 1920s without success. James Chadwick, who believed in the existence of the neutron, later remembered some of the attempts as "so desperate, so far-fetched as to belong to the days of alchemy" [3].

In these early developments theoretical physics played almost no role. This situation changed in the summer of 1928 when George Gamow proposed that α radioactivity could be understood in terms of quantum mechanics. He showed that the wave function of the α-particles extended outside the nucleus. Hence, the α-particle had a small but finite chance of sooner or later finding itself outside the nucleus; simply having "tunneled" through the nuclear outer surface.

During the following years, quantum mechanics proved instrumental in solving several other problems concerning atomic nuclei, such as γ emission and absorption, and inelastic effects in α-particle bombardments [3], but the efforts did not shed any light on the *structure* of the nucleus.

In the late 1920s several problems with the electron-proton model made electrons still necessary, but undesired in the atomic nucleus. In the textbook of Gamow from 1931, *Constitution of Atomic Nuclei and Radioactivity* (the first ever textbook in nuclear physics) he wrote: "The usual ideas of quantum mechanics absolutely fail in describing the behavior of nuclear electrons; it seems that they may not even be treated as individual particles" [4]. The neutron was still a missing particle, but the course of events that led to Chadwick's famed discovery of the neutron had already begun. In 1930, Walter Bothe and Herbert Becker discovered that beryllium exposed to α particles produced what they believed were energetic γ rays. Chadwick thought otherwise, the "beryllium radiation" might be Rutherford's neutron. He repeated and modified the experiments and his conclusion was that the radiation was not γ rays, but indeed neutrons [5].

In Heisenberg's important theory of nuclear structure of 1932-1933, in which he introduced exchange forces between the protons and neutrons, he treated the neutrons as a proton-electron compound. The neutron was a useful particle, because as Chadwick explained to the participants at the Solvay Congress in 1933, it could be used as a projectile in nuclear processes. He reported that he had observed α particles from neutrons reacting with oxygen. By 1934, electrons could finally be excluded from the nucleus.

During the year of 1932, not only the neutron was discovered, but also the

positron and deuteron. In May, 1932 Bohr wrote to Rutherford, "Progress in the field of nuclear constitution is at the moment really so rapid, that one wonders what the next post will bring .... One sees a broad new avenue opened, and one should soon be able to predict the behaviour of any nucleus under given circumstances" [6].

Nuclear physics, or rather nuclear speculations, entered astronomy at an early date. The new insight into the atomic constitution was first used in attempts to understand two classical mysteries of physics; *the production of energy in the sun and other stars* and *the creation of the elements*. The quantum mechanical theory of α decay lead to a new era of nuclear astrophysics. It became obvious that the tunneling process could be inverted and thus possibly explain the building up of elements by nuclear reactions. Still, it was first after 1932, following the discovery of the neutron, that the field of nuclear astrophysics began to deliver really promising results. In 1935 Gamow, making use of the new particle, the neutron, developed the idea that stellar element formation is based on neutron capture. These early ideas of neutron-induced nuclear processes did not lead to a satisfactory explanation of either *stellar energy production* or *element formation*.

The breakthrough with regard to stellar energy production came in 1939. Although he had no previous knowledge of astrophysics, Hans Bethe used his knowledge in nuclear physics to devise a detailed theory of solar energy production. At this time it was known that the most abundant element in nature is hydrogen, and that this is the main constituent of stars, making it likely that this element contributed to the energy production in stars. The essence of Bethe's work is that four protons fuse into a helium nucleus through a cyclic process wherein carbon nuclei act catalytically [7]. Contrary to earlier theories, Bethe's contribution was based on detailed calculations supplied with values of cross sections determined experimentally. The calculations Bethe performed of the central Sun temperature needed for the cyclic process to give the energy production was in excellent agreement with the one based on astrophysical models of the sun. Bethe's theory was not a theory of element formation, and therefore not directly relevant to the study of the synthesis of elements.

In 1938 Friedrich von Weizsäcker initiated a nuclear-archaeological program, attempting to reconstruct the history of the universe by means of hypothetical nuclear processes and to test these by the resulting pattern of element abundances. According to von Weizsäcker: "It is quite possible that the formation of the elements took place before the origin of the stars, in a state of the universe significantly different from today's" [8]. Gamow developed the program initiated by von Weizsäcker into a nuclear-physics based model of the early universe. Neither Gamow, Bethe, nor von Weizsäcker had any formal training in astronomy. They entered the field as nuclear physicists, confident in the power of nuclear and quantum theory.

In 1942 Gamow and other physicists concluded that a "Big Bang" was necessary in order to reproduce the element distribution known empirically from Victor Goldschmidt's work from 1937 [9,10]. This cosmological theory failed to explain the formation of elements heavier than helium. In spite of many attempts, they did not find a way to bridge the gaps at mass numbers 5 and 8, where no isotopes exists. But the failure did not lead to a dismissal of the theory, as it was at this time quite possible to assume that the other elements were results of later nuclear reactions in the interior of the stars.

A radical alternative to the Big Bang theory, the Steady State theory, was proposed in 1948 by Fred Hoyle, Hermann Bondi and Thomas Gold, also physicists without formal training in astronomy. They based their alternative theory on the postulate that the universe looks the same at any location and at any time and therefore the elementary matter is created continually throughout the universe. This theory provided the basis for a successful nuclear theory of the stellar origin of elements heavier than helium.

The problem of bridging the gaps at mass numbers 5 and 8 was solved in 1953 when Hoyle proposed the exited state of $^{12}_{6}$C, with energy of 7.7 MeV [11]. Such a state would have the same energy as the transient three α-particle combination, producing a "resonance" between the two states. This resonance should, theoretically, make the reaction about 10 million times more likely to occur. The predicted resonant state was quickly confirmed in experiments [12].

In an influential review, Suess and Urey presented a greatly improved distribution of observed solar-system abundances that showed several double peaks [13]. It was immediately clear that these abundance peaks were associated with the filling of neutron shells at the magic neutron numbers (50, 82 and 126) that Goeppert-Mayer and Jensen had presented in 1949 [14,15]. These discoveries made neutron capture a strong candidate in the synthesis of elements heavier than iron.

In 1952, the astronomer Merill detected spectral lines from the element technetium in evolved giant stars [16]. All of the technetium isotopes are unstable and the most long-lived isotope has a half life of $\approx 4.2 \times 10^6$y, quite short in a cosmological time scale. Consequently, the discovery served as a clear indication of an ongoing nucleosynthesis in the interior of stars.

Based on a large amount of experimental data, Burbidge, Burbidge, Fowler and Hoyle (B^2FH) published their milestone work on the synthesis of elements in stars in 1957 [17] (and independently by Cameron [18]). In this paper, the idea that all elements heavier than hydrogen can be built during the various evolutionary stages of stars was put forward. The authors postulated eight different nucleosynthetic processes giving a rather complete explanation for all details of the abundance curve. Nuclear species between ^{12}C and ^{56}Fe are produced in charged particle reactions; nuclear burning processes. Further fusion of charged nuclei *beyond the iron peak* is strongly suppressed due to the decreased binding energy per

nucleon, and the increasing Coulomb barrier. Thus, a different nucleosynthetic mechanism is required to account for those heavy elements. The *double* peaks in the abundance pattern at certain mass numbers corresponding to magic neutron numbers (A = 80 and 90, A = 130 and 138, and A = 195 and 208) gave rise to the idea of the synthesis of the heavy nuclei by two separate neutron-capture processes; the so-called slow neutron capture process (s-process) and the rapid neutron capture process (r-process). A third process, called the p-process, was also pointed out in B^2FH. The p-process is responsible for the production of a very small set of ≈35 naturally occurring proton-rich nuclei bypassed by the r- and s-processes.

In the next section, a brief summary of these three production modes will be given.

1.2 Nucleosynthesis beyond the iron peak

1.2.1 The s-process

The first direct evidence of the s-process came already from the observation of spectral lines of technetium in red giant stars as previously mentioned. These asymptotic giant branch (AGB) stars thus represent an excellent candidate for the s-process astrophysical site. In the s-process, neutrons are successively captured by the stable isotopes of a certain element until an unstable nucleus is reached. At this point the chain of neutron captures is terminated by β-decay, consequently producing the next nuclear species in the periodic table. The free neutron is unstable with a half-life $T_{1/2}$ = 615 seconds [19]. Thus a large amount of neutrons need to be continuously produced in the stellar environment to be available for neutron capture. The main sources of free neutrons are the $^{13}C(\alpha,n)^{16}O$ and $^{22}Ne(\alpha,n)^{25}Mn$ reactions [20], and the main starting point (seed) for the building of heavier elements is ^{56}Fe [20].

In the environments where the s-process takes place, the neutron densities are relatively low ($n_n \approx 10^8$ cm^{-3}). This ensures that the β-decay rate of an unstable nuclide formed in neutron capture exceeds the rate of the competing (n,γ) reaction: $\lambda_\beta \gg \lambda_{n\gamma}$. Thus, the reaction path follows the valley of β-stability (as shown in Fig. 1.1) and the s-process abundances are determined by the respective (n,γ) cross sections averaged over the stellar neutron spectrum (Maxwellian-averaged cross sections, MACS). Isotopes with a closed neutron shell, hence a significantly reduced neutron capture cross section, act as bottlenecks in the process path. This leads to increased abundance of isotopes with neutron magic numbers, N = 50, 82 and 126. The two abundance peaks corresponding to the last two magic numbers are shown in Fig 1.2. The s-process is extremely slow, with time scales of $\sim$ 1-100

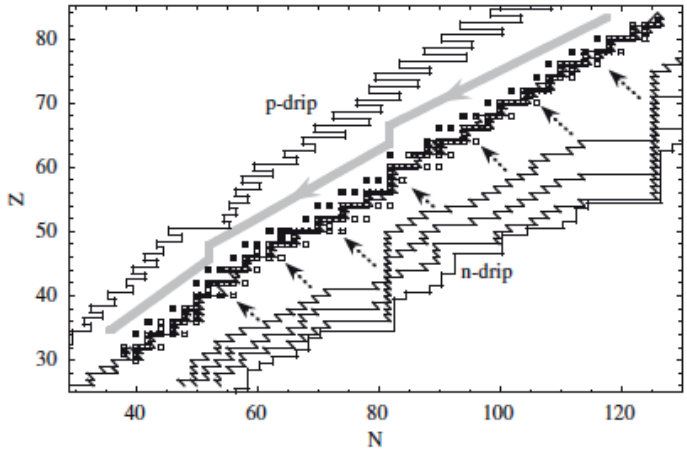

Figure 1.1: *Location in the (N,Z)-plane of the stable isotopes of the elements between Fe and Bi. The black squares are stable nuclides produced in the p-process and the open squares stable nuclides produced in the s-and/or r-process. The up-streaming s-process flow is confined to the valley of stability (thin jagged line). The up-streaming r-process flow is not well determined at present; three possible pathways are illustrated as zigzag lines on the neutron-rich side. Arrows indicate the β-decay path back to the valley of β stability. The down-streaming p-process path is also shown (grey line with arrows). The p- and n-drip lines give the approximate locations of zero proton and neutron energies. The figure is taken from [22].*

000 years, and terminates with the production of the heaviest stable nucleus ^{209}Bi.

At certain locations in the s-process path, unstable nuclei with β-decay rates comparable to the neutron capture rates; i.e. $\lambda_\beta \approx \lambda_{n\gamma}$ appear, splitting the s-process into two branches. The nucleus can at this point either capture a neutron or β-decay. The branching ratios of these processes are sensitive to the physical conditions at the stellar site, e.g. the neutron density [20]. The (n,γ) cross section of the branch point nuclei are usually inaccessible in direct measurements, due to their radioactive nature, although recent experimental improvements are promising in this respect [21]. In the work presented here, investigations have been made in order to obtain experimentally constrained (n,γ) cross sections for the s-process branch point nucleus, ^{147}Nd.

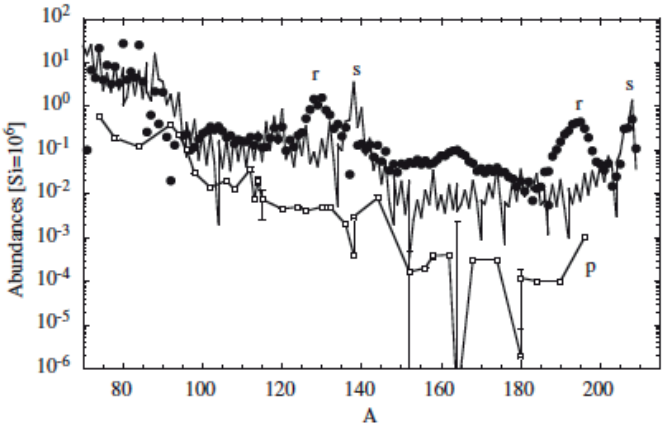

Figure 1.2: *Decomposition of the solar-system abundances of heavy elements into the s-process (solid line), r-process (filled circles), and p-process (open squares) nuclides. The "twin peaks" of the r- and s-processes between mass A ≈ 120-140 and 185-210 are clearly seen. The figure is taken from [22].*

1.2.2 The r-process

Since the s-process terminates at ^{209}Bi, it is clear that this process is not accountable for the production of all heavy isotopes in the solar abundance distribution, such as the very long lived radioactive nuclides ^{232}Th, ^{235}U and ^{238}U. Taken together with the observed abundance peaks at mass A = 130 and 195 (see Fig. 1.2), this clearly indicates an additional neutron capture process, called the r-process. This process operates under very different conditions compared to the s-process. It is thought to occur on very short time scales on the order of a few seconds and with very high neutron fluxes ($n_n \gg 10^{20}$ cm^{-3}) [20]. The high neutron exposure drives the matter to the neutron-rich side of the nuclear chart, as seen in Fig. 1.1, where the abundances of magic nuclides with filled neutron shells accumulate. When the neutron flux is exhausted, these magic nuclides will β-decay along the isobaric chains until the most neutron-rich stable (or very long lived) nucleus is reached [20]. Therefore, the r-process mass peaks are located at lower mass than the s-process peaks, as seen in Fig. 1.2. To account for the production of nearly half the isotopes heavier than iron, we need the r-process. Still, the astrophysical conditions such as the site of the process, is not unambiguously determined [22]. Different extreme scenarios have been proposed, such

as core-collapse supernovae [22], neutron-star mergers, ν-driven wind [22] and ejected matter from accretion discs around black holes [23, 24]. However at the moment the favored site for the r-process is the ν-driven wind for the weak r-process (primarily forming the A$\sim$80 abundance peak), and neutron-star mergers for the strong r-process (responsible for producing A $\approx$ 130 and heavier isotopes). The abundances of the stable r-nuclides are determined by the cross sections of the exotic, neutron-rich nuclei far from the stability line. A large-scale r-process abundance calculation requires a nuclear network of about 5000 isotopes. Furthermore, information on as much as 50 000 reaction rates are needed as input. The vast majority of the neutron-capture cross sections are inaccessible for direct measurements, and a robust theoretical description with high predictability is therefore required. The uncertainty in the theoretical predictions of (n,γ) reactions used in the r-process models can be as large as a factor of 100-1000 [25]. Therefore, experimental constraints on these neutron capture reactions are of great importance and have been addressed in the case of Ni and Ge in the work presented here.

1.2.3 The p-process

A few stable proton-rich isotopes ($\approx$35) cannot be produced in the s- or the r-processes. These are called the p-nuclei; ^{74}Se being the lightest and ^{196}Hg the heaviest. These rare nuclei are also underproduced in comparison to isotopes of the same element produced in the s- and r-processes, visualized in Fig. 1.2. In all proposed scenaria of the p-process [26], the nucleosynthesis occurs at high stellar temperatures, between 1.8 and 3.3 GK, but the favoured site of the p-process is explosive O/Ne-shell burning in massive stars. In these environments, p-nuclei are produced in a series of neutron, proton, and α-particle photodisintegrations, their inverse capture reactions and/or β^+ decays. This ensemble of reactions is illustrated in Fig. 1.3. Missing in this figure is the destruction of the p-nucleus. Because the p-nuclei are extremely low in abundance, this event becomes important and should be accounted for [27].

Somewhat similar to the r-process, abundance calculations for the p-process require the solution of a large network of about 2000 nuclei (the majority of which are unstable) and more than 20 000 nuclear reactions. Hence, it is impossible to determine all these nuclear reaction rates experimentally. As a consequence, the network calculations have to rely on theoretical predictions of the cross-sections.

At present, all the models of p-process nucleosynthesis are able to reproduce most of the p-nuclei abundances within a factor of 3, but fail in the case of the light p-nuclei [28]. Uncertainties in the astrophysics modeling of the p-process can lead to such discrepancies, as can the poor knowledge of nuclear properties.

For a more in-depth description of the p-process, see Refs. [26, 27]. In this work, the destruction of the p-nucleus ^{144}Sm in photodissosiation and the produc-

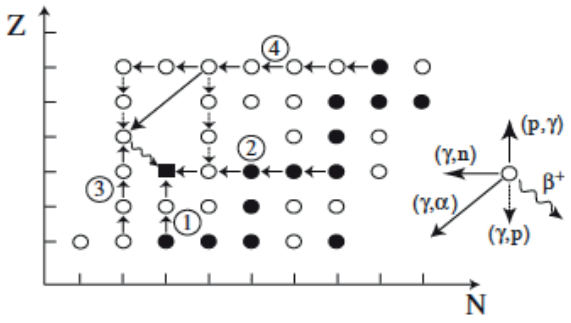

Figure 1.3: *The possible routes for the formation of one p-nuclide (black square) from seed nuclei (black dots). Note that the important process of destructing the p-nuclide is not included in the figure. The figure is taken from Ref. [26].*

tion of the p-process ^{146}Sm chronometer [29] was studied.

1.3 Nuclear physics

One contemporary and exciting example of how fundamental research in nuclear physics is implemented in nuclear astrophysical research is within the exploration of neutron capture cross-sections, which are relevant for the aforementioned processes (s- and r-processes).

1.3.1 Radiative neutron capture

Direct measurements of neutron capture cross sections for relatively high incoming neutron energies ($\approx$ keV) are quite challenging. Unfortunately, in astrophysical environments the energy of the neutrons fall within this range, $\approx$ 9-900 keV (corresponding to stellar temperatures of 0.1-10 GK). Measurements prove even more challenging in the case of unstable isotopes, since radioactive targets are difficult to handle and have a high intrinsic radiation. Therefore, statistical models are commonly utilized in lieu of direct measurements. To describe radiative neutron capture, the statistical framework provided by the Hauser-Feshbach model [30] is utilized. The model is applicable for compound nuclei with a statistical distribution of nuclear excited states, and the neutron capture cross section

can be expressed as:

$$\sigma_{n,\gamma} = \frac{\pi}{k_n^2} \sum_{J,\pi} g_J \frac{\mathscr{T}_\gamma(E,J,\pi)\mathscr{T}_n(E,J,\pi)}{\mathscr{T}_{\text{tot}}} \approx \frac{\pi}{k_n^2} \sum_{J,\pi} g_J \mathscr{T}_\gamma(E,J,\pi), \tag{1.1}$$

where k_n represents the incident neutron wave number, E, J and π gives the energy, spin and parity of the compound state; $\mathscr{T}_\gamma$ and $\mathscr{T}_n$ are the γ- and neutron-transmission coefficients, respectively, and $\mathscr{T}_{\text{tot}} = \mathscr{T}_\gamma + \mathscr{T}_n$. The factor g_J is given by $g_J = (2J+1)/(4J_t+2)$, where J_t is the spin of the target nucleus. In the case of keV neutrons, the decay from states above the neutron separation energy, S_n, is dominated by the neutron emission channel. Thus, the γ-transmission coefficient is significantly smaller than the neutron-transmission coefficient ($\mathscr{T}_\gamma << \mathscr{T}_n$). This means that $\mathscr{T}_n(E,J,\pi) \approx \mathscr{T}_{\text{tot}}$, allowing the approximation in Eq. (1.1).

The γ-transmission coefficient is given as

$$\mathscr{T}_\gamma(E,J,\pi) = \sum_{\nu,X,L} \mathscr{T}^{\nu}_{XL}(E_\gamma) + \sum_{X,L} \int \mathscr{T}_{XL}(E_\gamma)\rho(E-E_\gamma,J,\pi)dE_\gamma, \tag{1.2}$$

where $\mathscr{T}_{XL}(E_\gamma)$ is the γ-transmission coefficient for energy E_γ with multipolarity XL, and ρ represents the nuclear level density [31]. The first term is a sum of $\mathscr{T}_{XL}$ over low-lying discrete states ν relevant to a given multipolarity (XL) and the second term is an integration of $\mathscr{T}_{XL}$ over nuclear states $\rho(E-E_\gamma)dE_\gamma$ in the energy interval dE_γ at the excitation energy $E-E_\gamma$. The γ-transmission coefficient is uniquely related to the downward γ-ray strength function $\overleftarrow{f_{XL}}(E_\gamma)$ by $\mathscr{T}_{XL}(E_\gamma) = 2\pi E_\gamma^{(2L+1)} \overleftarrow{f_{XL}}(E_\gamma)$. The radiative neutron capture cross-section is dependent upon three nuclear statistical quantities: nuclear level density (NLD), γ-ray strength function (γSF) and neutron-nuclear optical potential. Of these three quantities, the uncertainties of NLD and γSF have the largest impact on calculated radiative neutron capture rates. The lack of experimental data on NLDs and γSFs of unstable nuclei warrants theoretical approaches. To test and improve the predictive power of such theoretical calculations, it is necessary to provide reliable experimental data for those reactions which we are in fact able to study in the laboratory. A brief overview of theoretical and experimental approaches to NLDs and γSFs is presented here.

1.3.2 Nuclear Level Density

NLD is defined as the number of quantum levels in a nucleus per energy unit as a function of excitation energy. Various models are employed to calculate the NLD, the most commonly used being the so-called Fermi gas model. In the first version of this model, introduced by H. Bethe already in 1936 [32], the NLD was

described as a gas of non-interacting fermions moving in equally spaced single-particle orbitals. The original formula has been modified several times alongside developments in theoretical nuclear physics. The current back-shifted Fermi gas model has been the most common description of NLD for decades and is given by:

$$\rho_{BS}(E) = \frac{\exp[2\sqrt{a(E-E_1)}]}{12\sqrt{2}\sigma a^{1/4}(E-E_1)^{5/4}}, \tag{1.3}$$

for an excitation energy E, where the level density parameter a and the energy shift E_1 are treated as free parameters that can be fitted to experimental data. The spin-cutoff parameter can be parameterized in several ways. The two preferred approaches are given by von Egidy and Bucurescu, see Refs. [33, 34].

Another commonly used expression for the NLD is the constant-temperature model [35]:

$$\rho_{CT} = \frac{1}{T_{CT}}\exp\frac{E-E_0}{T_{CT}}, \tag{1.4}$$

where T_{CT} is determined by the slope of $\ln \rho(E)$.

Other approaches to theoretically establishing the NLD are the Hartree-Fock-Bogoliubov (HFB) plus combinatorial model of S. Goriely [36] and the temperature-dependent model of S. Hilaire [37], as well as the shell-model Monte Carlo approach [38–40].

When it comes to probing the NLD experimentally, several methods have been developed and applied in various excitation energy regions. Below S_n, NLD can be extracted from evaporation spectra using Hauser-Feshbach modeling [41]. Lately a new method based on high-resolution studies of $E2$ and $M2$ giant resonances [42] gives information on the spin and parity-dependent NLD. Another method to measure the NLD has been developed by the Oslo nuclear physics group [43]. The essence of this method is a statistical analysis of primary-γ spectra extracted from various excitation bins and a simultaneous extraction of NLD and γSF. A more detailed description of models and calculations of NLDs is provided in [44].

1.3.3 Gamma-ray Strength Function

The γSF characterize the average electromagnetic properties of excited nuclei. The original definition of a model-independent γSF is given by [45]

$$f_{XL}(E_\gamma) = \frac{\langle \Gamma_{\gamma l} \rangle}{(E_\gamma^{2L+1} \mathrm{D}_l)} \tag{1.5}$$

where $\langle \Gamma_{\gamma i f} \rangle$ is the average radiative width, E_γ gives the transition energy and D_l represents the level spacing of the initial states.

Both γ-decay and photo-absorption processes are described through γSFs. We distinguish between the corresponding types of γSFs [44],

(i) Downward strength function $\overleftarrow{f}$ expressed in terms of the average radiative width of γ decay.

(ii) Photo-excitation (upward) strength function $\overrightarrow{f}$ related to the γ absorption cross-section.

The γSF is closely connected to the γ-transmission coefficient $\mathscr{T}_{XL}$:

$$\mathscr{T}_{XL}(E_\gamma) = 2\pi E_\gamma^{2L+1} \overleftarrow{f_{XL}}(E_\gamma). \tag{1.6}$$

which represents a transition with multipolarity XL and energy E_γ. The upward γSF is given by [44],

$$\overrightarrow{f_{XL}}(E_\gamma) = \frac{1}{(2L+1)(\pi\hbar c)^2} \frac{\left\langle \sigma_{\mathrm{XL}}(E_\gamma) \right\rangle}{E_\gamma^{2L-1}}, \tag{1.7}$$

where the average photo-absorption cross section $\left\langle \sigma_{\mathrm{XL}}(E_\gamma) \right\rangle$ is summed over all possible spins of the final states.

According to Fermi's golden rule and the principle of detailed balance, the upward and downward γSF will correspond to each other, given that the same states are populated equally whether they are populated from above or below. This requirement is generally not completely met.

A microscopic treatment of the γSF is necessary to have predictive power throughout the nuclear chart. Several publications have been dedicated to the microscopic description of γSF. Shell-model calculations have recently been used to calculate the $M1$ and $E2$ component of the γSF (Refs. [46–48]). The quasi-particle random phase approximation (QRPA) method has proven successful in reproducing experimental data [49]. Recently, quasi-particle time-blocking approximation (QTBA) calculations, coupling the single particle degrees of freedom to the phonon degrees of freedom, have proven to reproduce the pygmy resonances observed in e.g. Sn and Ni isotopes [50, 51].

By far the largest contribution of experimental information on the γSF is from photo-absorption measurements [44]. Recently, an improved measurement technique has been developed with the emergence of quasi-monoenergetic photon beams produced in laser Compton-scattering reactions [31]. Below neutron separation energy, measurements of γSFs have proven quite challenging, but some techniques have been successful, such as the Nuclear Resonance Fluorescence (NRF) method [52], fitting of multiplicity spectra [53] and the Two-Step Cascade (TSC) method [54]. Recently a method permitting measurements of the γSF (and

NLD) across S_n using polarized proton scattering has been devised [55]. The Oslo method makes it possible to extract the γSF below S_n through a statistical analysis of excitation energy indexed primary γ-ray spectra. A more detailed description of models and calculations of γSFs is provided in [44].

1.4 The low-energy enhancement

The contrast between the first predictions on the γSF [56] (where the γSF was considered to be independent of γ energy) and the present picture of this entity is striking. It is now clear that structures in the γSF can provide valuable information on nuclear degrees of freedom and underlying dynamics. The strength of the isovector Giant Electric Dipole Resonance (GEDR) [57], which originates from a collective vibration of the neutron system against the proton system, overshadows all other decay modes of the nucleus for $E_\gamma \approx 12-17$ MeV. In the energy region well below the centroid of the GEDR, fine structures in the γSF have been revealed. For example, two types of magnetic dipole, $M1$, resonances have been discovered. The scissors mode, predicted by [58], is caused by the deformation degree of freedom, allowing the neutron and proton clouds to "clip" against each other like a pair of scissors. This resonance generates a bump in the $M1$ strength around 3 MeV in deformed nuclei [59–61]. Lately, radiative neutron-capture rates are calculated with and without the scissors mode for neutron-rich Fe, Ge, Kr, Sr, Ru, and Te isotopes [62]. If one includes the scissor mode, the calculations show a strong enhancement in (n,γ) rates for very neutron-rich isotopes. At higher energies, typically around 8 MeV, the $M1$ strength is dominated by the spin-flip resonance [59]. As for the $E1$ part of the γSF apart from the GEDR, it is dominated by a pygmy resonance experimentally measured from γ-ray energies close to the neutron separation energy in stable as well as unstable, neutron-rich nuclei [63–66]. Such a resonance is predicted on the basis of a neutron "skin" oscillating against an N$\approx$ Z core. There is nevertheless disagreement as to whether the $E1$ pygmy is in fact caused by the collective phenomenon of a neutron-skin oscillation, or whether it is caused by single- or few-particle excitations that happen to give a concentrated $E1$ strength close to S_n. This extra strength could significantly affect the (n,γ) cross section in nuclei in which it is found [67], such as for s-process branch point nuclei, and could potentially change the outcome of the large-scale network abundance calculations on the r-process [68].

Recently, an unexpected enhancement of the γ decay probability at very low γ energies (below 3 MeV) have been observed in many fp shell and A $\sim$ 90-100 nuclei, using the Oslo method. In what follows, a short chronological synopsis of this low-energy enhancement will be presented.

In 2004, the low-energy enhancement was first reported in ^{3}He-induced reac-

tions on ^{57}Fe [69]. In the same publication, the low-energy enhancement found in ^{57}Fe was confirmed using the TSC method. In the following year, an extensive study of Mo isotopes between ^{93}Mo -^{98}Mo was published [70]. All six isotopes studied exhibited the same low-energy enhancement in their γSF as found in ^{56,57}Fe. By this point, this newfound low-energy enhancement had attracted international scientific attention, inspiring other groups to independently investigate the γSF at low γ energies in the search for this phenomenon. An experiment using thermal neutron capture on ^{95}Mo, analyzed using the TSC method [71] did not reproduce the low-energy enhancement. Another experiment analysing γ ray cascades following neutron capture on ^{95}Mo was performed with the γ calorimeter at DANCE [53]. The essence of their findings is summed up in this quote: "The data are not consistent with the large enhancement of the PSF (γSF) proposed by the Oslo group. However our experimental data are not sufficiently sensitive to distinguish between a *small* low-energy enhancement and *no* enhancement". A good overview of the situation at this point is given in Ref. [72].

At the time, neither the type (magnetic, electric) nor the multipole of this observed structure was known, as the Oslo method does permit disentanglement of different types and multipoles of the γSF. In addition, there was at this point no theoretical understanding of the underlying mechanisms of the structure. The natural course of action, then, was to continue measuring the γSF of other light nuclei in the hopes of mapping the phenomenon. During the next few years data on the γSF of V [73], Sc [74], and Ti [75–77] isotopes displayed the low-energy enhancement.

In an article published in 2010 [78], the low-energy enhancement structure was again observed, in ^{60}Ni. This time, Voinov *et al.* used an improved version of the TSC method to extract the γSF of ^{60}Ni from data obtained in the ^{59}Co(p, 2γ)^{60}Ni reaction in order to reduce the uncertainties associated with the procedure for neutron capture reactions. To additionally improve the reliability of the extracted γSF, NLD of ^{60}Ni had been measured prior to the experiment utilizing neutron evaporation spectra. While the data analyzed in this article showed strong indications that the enhancement is due to $M1$ transitions, the authors were careful to draw any general conclusions, as ^{60}Ni is in many ways a special case. It has only positive-parity states below excitation energies of ≈ 4.5 MeV. This fact has significant consequences for the TSC method employed in Ref. [78], as it means that for the secondary γ ray, $M1$ transitions are strongly enhanced compared to $E1$ transitions, thus rendering it impossible to conclude anything regarding the type of the low-energy enhancement. Besides being an intriguing new nuclear-physics phenomenon in itself, the low-energy enhancement was shown to have the potential to influence the astrophysical (n, γ) reaction rates. In Ref. [79] it was demonstrated for the first time that the low-energy enhancement could cause a 2 orders of magnitude increase in the astrophysical r-process reaction rates for very

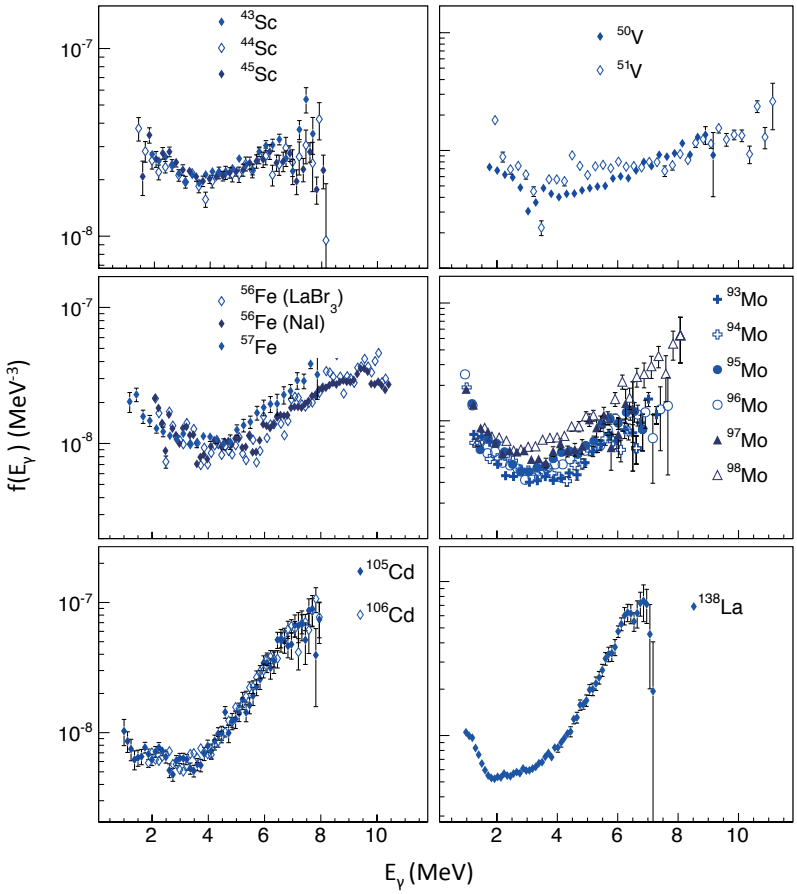

Figure 1.4: *Low-energy enhancements identified using the Oslo method anno 2015. The data are retrieved from Ref. [84].*

neutron-rich nuclei.

In 2012, the existence of the low-energy enhancement was independently confirmed using a different set-up and extraction technique for ^{95}Mo [80], using proton-γ-γ correlations from the ^{94}Mo(d, p)^{95}Mo reaction, populating not only the area around neutron binding energy but the whole quasi-continuum range. As for the mass range within which the low-energy enhancement had until this point been

observed, it was believed that Cd constituted a transitional nucleus, exhibiting low-energy enhancement for lighter but not heavier isotopes of that element. In the following year, the case of ^{56}Fe was revisited [81] and the low-energy enhancement confirmed using large volume $LaBr_3$ scintillation detectors. From studies of the angular distributions of the emitted γ rays, it was proved that the low-energy enhancement is dominated by dipole transitions in ^{56}Fe. Almost immediately after the multipole of the low-energy enhancement was established for ^{56}Fe, two theoretical descriptions of the low-energy enhancement were published. The work of Litvinova and Belov [82] for ^{94,96,98}Mo within the thermal continuum quasiparticle random phase approximation predicts an electric ($E1$) character, while shell-model calculations for $^{94-96}$Mo and ^{90}Zr by Schwengner *et al.* [47] give a strong enhancement for low γ-ray $M1$ transitions due to a re-coupling of high-j proton and neutron orbits. Recent large basis shell-model calculations on ^{56,57}Fe by Brown *et al.* [48] show again a large increase of the $M1$ strength for low γ-ray energies, further supporting the $M1$ nature of the low-energy enhancement. The dominant mechanism is found to be $0\hbar\omega$ transitions within the f-shell. It follows that because these $0\hbar\omega$ transitions should be present in all nuclei, the low-energy enhancement would be expected throughout the nuclear chart. A finding that supports this theory is the recently reported low-energy enhancement in ^{138}La [83]. See Fig. 1.4 for a compilation of low-energy enhancements discovered using the Oslo method.

1.5 Experimental efforts and theoretical approaches

The goal of this thesis was primarily to extract the NLD and the γSF from experimental data. Recently, exotic, neutron-rich Ni and Ge isotopes were pointed out in a sensitivity study, to highly influence the outcome of the weak r-process [25]. The relevant isotopes are shown in Figs. 1.6 and 1.7. If structures in the γSF of stable nuclei are also found in more exotic neutron-rich neighbours, they may greatly effect the neutron capture cross sections. Efforts are indeed taken to approach these exotic nuclei experimentally. But until that goal is reached, we consider the careful measurements of the statistical properties of stable Ni and Ge isotopes to be of great value.

Various experimental techniques have been used to investigate γSFs, such as γ-scattering experiments, neutron-induced two-step cascade measurements, charged-particle induced reactions and photo-neutron reactions. In contrast to what one might expect, these measurements have differed in shape and absolute value. Molybdenum-96, which has been thoroughly investigated, provides a good example of these discrepancies (See Fig. 1.5).

These unsettling findings inspired a collaboration to systematically investigate

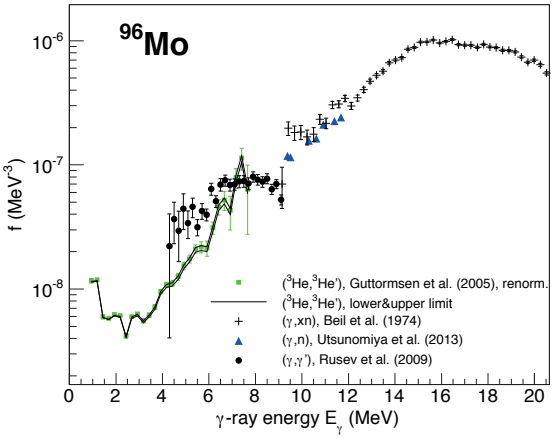

Figure 1.5: *Gamma-ray strength function, $f(E_\gamma)$, extracted from photon-scattering measurements, from charged-particle induced reaction data and from photo- neutron reactions. The figure is taken from [90].*

the γSF of one specific nucleus, ^{74}Ge, using a wide variety of reactions and methods for analysis. In this collaboration, the γSF of ^{74}Ge was extracted from data obtained in five different reactions; ^{74}Ge(γ,γ') at γELBE [85], ^{74}Ge$(p,p'\gamma)$ at Berkeley [86], ^{74}Ge$(\alpha,\alpha'\gamma)$ at iThemba LABS [87], ^{74}Ge(^{3}He, ^{3}He$'\gamma$) at OCL [88] and ^{74}Ge(γ, n) at NewSUBARU [89] in a time period between 2012 and 2013. As a part of this collaboration I performed two of these five experiments, the ^{74}Ge (^{3}He, ^{3}He$'$) at OCL and the ^{74}Ge(γ, n) at NewSUBARU, the results of which are presented in this thesis. The charged-particle reaction lets us also investigate ^{73}Ge from the neutron pick-up reaction ^{74}Ge(^{3}He, $\alpha\gamma$). Applying the Oslo method to the data obtained with the ^{74}Ge(^{3}He, ^{3}He$'\gamma$) reaction, both NLD and γSF were extracted. The photoneutron dataset gave the γSF above the neutron separation energy, and, together with the OCL data, covers a range between $\sim$ 1.5-13 MeV in γ energy. Shell-model calculations of the $M1$ part of the γSF have been performed and compared with the experimental findings. Radiative neutron-capture cross sections of ^{72,73}Ge have not previously been measured, and could for the first time be constrained.

Recently, a new experimental technique called the β-Oslo method, based on the traditional Oslo method, has been devised. This method has a goal of constraining the neutron capture cross section of neutron-rich, unstable nuclei. The

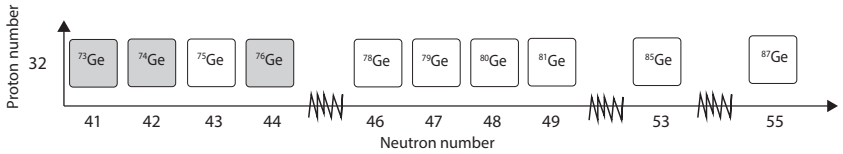

Figure 1.6: *Germanium isotopes of interest in the current work. The isotopes* ^{73,74,76}*Ge have been investigated experimentally and (n,*γ*) cross sections deduced for* ^{72,73,75}*Ge for the first time. The very neutron-rich isotopes,* ^{81,85,87}*Ge are assumed to be of vital importance in the r-process.*

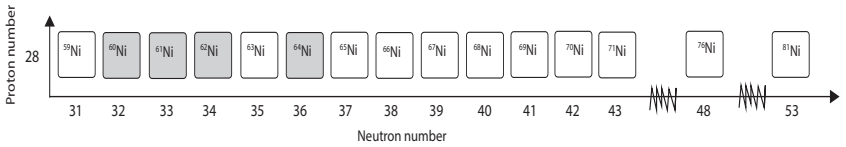

Figure 1.7: *Nickel isotopes of interest in the current work. The isotopes* ^{59,60}*Ni have been investigated experimentally in this work and* ^{64,65}*Ni are currently under analysis using the Oslo method. Recent results on* ^{68}*Ni shows a strong pygmy resonance (see Refs. [66, 91]). The neutron-rich* ^{70}*Ni was reached in a recent experiment using the* β*-Oslo method.*

first experimental results from this method, where γ spectra from the β-decay of ^{76}Ga were analysed and the capture cross section of ^{75}Ge could be strongly constrained, are presented in this thesis. This is a first step towards obtaining experimental data on the elusive, unstable isotopes involved in the r-process. Shown in Fig. 1.6 are the stable Ge isotopes investigated in this work and the exotic isotopes we aim to study in the future.

The reported low-energy enhancement in the γSF of ^{60}Ni [78] already discussed in Sec. 1.4 provided a strong motivation to investigate the γSF from another perspective: i.e. performing a charged-particle induced reaction on a ^{60}Ni target and inferring the NLD and γSF using the statistical analysis of the primary γ-ray spectra of the following decay. Shell-model calculations of the $M1$ component of the γSF have been performed. Not only the very low-energy enhancement, but also a higher lying resonance, the pygmy resonance, is interesting in the case of Ni isotopes. It has been seen experimentally in Ref. [66] that there is a strong pygmy resonance in the neutron-rich ^{68}Ni. Theoretically, this enhancement in

$E1$ strength around neutron separation energy is not reproduced in quasi-particle random phase approximation (QRPA) calculations. However, quasi-particle time blocking approximation (QTBA) calculations [51], have successfully reproduced this enhancement. QTBA calculations are performed for ^{60}Ni as a part of this work, and compared with the experimentally measured γSF. Data obtained at OCL on ^{64,65}Ni are currently under analysis by the Oslo group.

The first dedicated β-Oslo experiment was performed in 2015. As a part of a major effort to map the features of the NLD and γSF of a range of stable and unstable isotopes, we obtained data on the neutron-rich ^{70}Ni. As shown in the aforementioned sensitivity study [25], reaction rates of extremely neutron-rich Ni isotopes, such as ^{76}Ni and ^{81}Ni might have a large effect in the weak r-process, thus encouraging continued investigations of neutron-rich Ni isotopes. Shown in Fig. 1.7 are the stable isotopes investigated in this work and the exotic isotopes we seek to study in the future.

As mentioned, the main challenge in connection with the modeling of the s-process flow is the appearance of unstable isotopes which leads to a possible branching of the pathway. In the rare-earth region several such important nuclei exist, e.g. ^{147}Nd with a half-life of 10.9 d. Due to the short half-life of this branch-point nucleus, direct measurements of the neutron-capture cross sections prove impossible. Therefore, an indirect method, called the γSF method [31], has been used in an effort to constrain the neutron-capture cross section of ^{147}Nd. In addition neutron-capture cross section of the very short-lived ^{153}Sm has been constrained for the first time. A series of photoneutron measurements on stable Sm and Nd isotopes have been performed as a means of accomplishing this goal. See Fig. 1.8 for an illustration of the measured and deduced quantities from the experiments. These extensive measurements also include the destruction of the p-nucleus ^{144}Sm and the creation of the p-nucleus ^{146}Sm.

This thesis is an article-based thesis; therefore only a rather short description of the theoretical considerations and the experimental details are given. The presented work is organized as follows: in chapters 2 and 3, experimental techniques and methods are discussed. The full scientific work is described in the papers presented in chapter 4. Finally, a summary, as well as a discussion of important issues and an outlook are given in chapter 5.

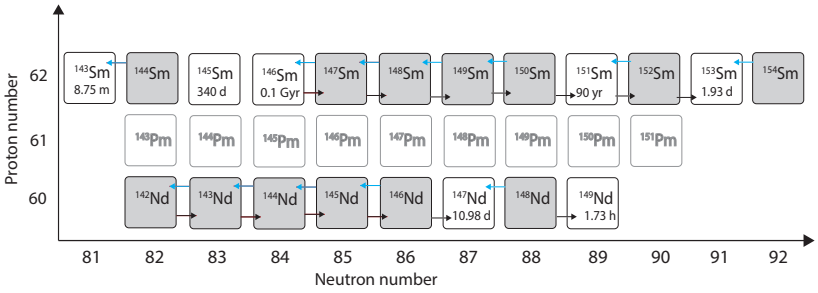

Figure 1.8: *A section of the chart of nuclei illustrating the systematic analysis of (γ, n) and (n, γ) cross sections for Nd and Sm nuclei. The blue left-pointing arrows show photoneutron cross sections that have been measured in the present experimental campaign. Radiative neutron-capture cross sections evaluated in the present systematic analysis are shown by right-pointing arrows. Stable isotopes are shown as gray boxes, and unstable isotopes are shown as white boxes (with their terrestrial half-lives).*

Chapter 2

Experimental details and data analysis

In this work, γSFs have been deduced using three different experimental techniques: charged-particle induced reactions, β-decay experiments and photoneutron experiments. From the first two methods the NLDs can be extracted as well. A short overview of the individual techniques is given in the following.

2.1 Charged-particle induced reactions

The experiments were performed at the Oslo Cyclotron Laboratory (OCL) at the University of Oslo, between 2010 and 2012. An MC-35 Scanditronix cyclotron was used to deliver pulsed light-ion beams, see Table 2.1 for a list of available beams. The cyclotron has been in operation since 1979, and has until recently been used in production of the radioactive isotope ^{18}F used in medical diagnostics at the Norwegian Radium Hospital in Oslo. Today, the cyclotron is mainly used for basic research within nuclear physics and chemistry.

In both the nickel and the germanium experiments presented in this thesis, a ^{3}He beam of 38 MeV with a radiofrequency of 15.3 MHz was used. In order to avoid pileup in the detectors, the beam current was limited to $\approx$ 0.3-0.7 enA. The ^{60}Ni and ^{74}Ge targets were both self-supporting with a thickness of 2 mg/cm^2 and 0.5 mg/cm^2 respectively. The target used in the Ge experiment at OCL was also used in a complimentary (α, $\alpha^{'}\gamma$) experiment at iThemba LABS. The enrichment of the ^{60}Ni target was 99.9%, whereas the enrichment of the ^{74}Ge target was estimated to be >90%. The duration of the two experiments were $\approx$ seven days each.

Ion	Charge state	Energy range (MeV)	Intensity (μA)
Proton	$^{1}H^{+}$	2-35	100
Deuteron	$^{2}H^{+}$	4-18	100
Helium-3	$^{3}He^{++}$	6-47	50
Helium-4	$^{4}He^{++}$	8-35	50

Table 2.1: Beams available at the Oslo Cyclotron Laboratory.

2.1.1 Experimental setup

The targets were irradiated with a beam of of 38 MeV ^{3}He particles. The inelastic (^{3}He, ^{3}He$'\gamma$) reaction and the neutron pick-up (^{3}He, $\alpha\gamma$) reaction were studied. The corresponding Q-values for the reactions are given in Table 2.2. Particle-γ coincidences were measured with the CACTUS γ-ray array [92], and the Silicon Ring (SiRi) particle telescope system [93]. An illustration of the particle-γ coincidence detection set-up is shown in Fig. 2.1. A schematic overview of the laboratory is given in Fig. 2.2. When the beam of ^{3}He particles reaches the location labeled CACTUS, it has been focused and collimated to a diameter of $\approx$ 1-2 mm. SiRi is a composite system consisting of 8 trapezoidal-shaped silicon detector modules put together to form an approximate ring, see Fig. 2.3 a). Each of the modules consist of a 130-μm thick ΔE detector, segmented into 8 curved strips. Each ΔE strip is placed in front of a 1550-μm thick E detector. The SiRi can be placed in both forward and backward direction, covering angles relative to the beam axis from θ=40° to 54° and θ=126° to 140°, respectively. Each strip covers an angle of 2°. In front of the detector modules, a 10.5 μm thick aluminum foil is placed to shield the ΔE detectors from δ electrons and light. The SiRi system is placed inside the target vacuum chamber and the center of the detector modules are located at a distance of 5.0 cm from the target, as shown in Fig. 2.3 b). SiRi

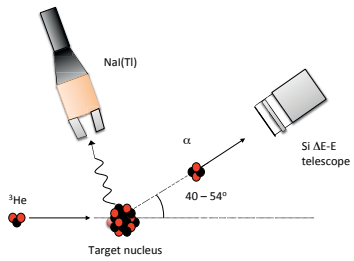

Figure 2.1: *Schematic set-up for particle-γ detection.*

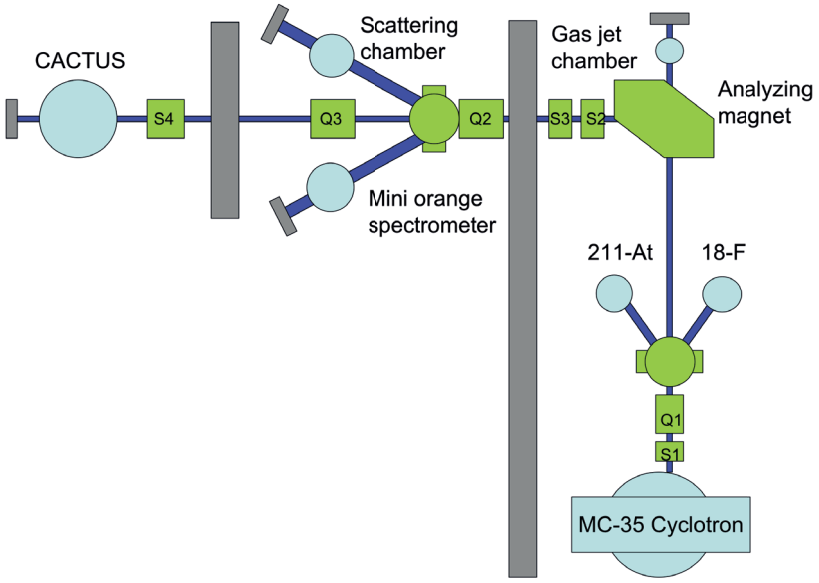

Figure 2.2: *An overview of OCL with its target stations. The figure is taken from [88].*

has a solid angle coverage of ≈ 8 % of 4π.

The γ-ray detection system CACTUS consists of 28 NaI:Tl detectors of size $5'' \times 5''$. The individual NaI detectors are distributed on a spherical frame in a distance of 22 cm from the target. To reduce cross-talk between the NaI crystals, they are covered with lead collimators, reducing their exposed diameter from 12.7 cm to 7 cm. The total efficiency of the CACTUS array is 15.2 % and the full-width half maximum energy resolution is ≈ 6 % for γ-rays of 1.3 MeV. CACTUS has a solid angle coverage of ≈ 18 %. The γ-detection system is named after its appearance, which can be seen from Fig. 2.4. Since our aim is to study particle-γ coincidences stemming from the same nuclear reaction, we need to measure the following:

(i) The time between the detection of a particle and a γ-ray.

(ii) The particular ejectile of interest in the reaction.

(iii) The γ ray spectra in coincidence with the charged-particle ejectiles of inter-

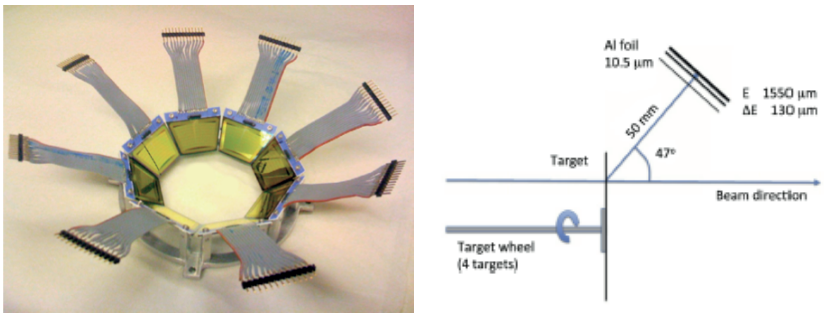

(a) (b)

Figure 2.3: *The SiRi detector system. (a) A photo of the system and (b) the position of SiRi inside the target chamber. The figures are taken from Ref. [93].*

est.

How these requirements are met will be discussed here.

2.1.2 Coincidence technique

The E back segments of the SiRi detector system were used as master-gates and as the start signal for the time-to-digital-converter (TDC). Individual TDC stops were given from one or more of the NaI detectors in the event of γ detection. An ejectile and a γ-ray stemming from the same nuclear reaction will in principle reach SiRi and the NaI detector almost simultaneously, but the stop signal is delayed by $\approx$ 400 ns in order to create a small time interval where measurements are accepted. A typical time spectrum is shown in Fig. 2.5. The peak centered at $\approx$ 400 ns corresponds to events with practically no time difference (the time resolution is typically $\approx$ 15-20 ns) between particle and γ detection. The smaller peaks on each side of the prompt peak stem from false coincidences between particles and γ rays from different beam pulses. In addition, we assume that there will be an even distribution of false coincidences underlying the peak structures. In the analysis, the background is subtracted by gating on the prompt peak in the time-spectrum and subtracting the events obtained from gating on one of the background-peaks, as shown in Fig. 2.5.

2.1.3 Particle-γ matrix

When the ^{3}He beam impinges on the target, multiple reaction-channels are opened, such as (^{3}He, xnγ), (^{3}He, pγ), (^{3}He, ^{3}Hγ), and (^{3}He, ^{3}He$'\gamma$). The energy loss of a

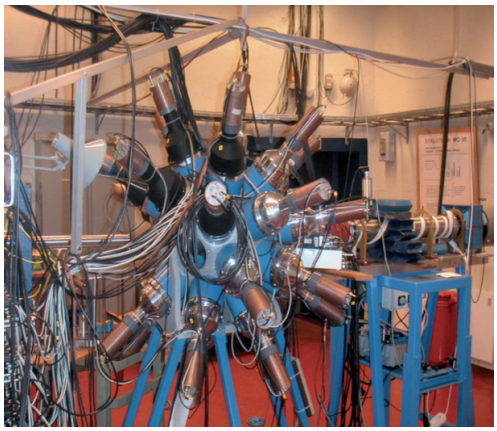

Figure 2.4: *The γ-detector array CACTUS.*

Nucleus	Reaction	Q-value (MeV)
^{59}Ni	^{60}Ni(^{3}He, $\alpha\gamma$)	9.19
^{60}Ni	^{60}Ni(^{3}He, ^{3}He γ)	-
^{73}Ge	^{74}Ni(^{3}He, $\alpha\gamma$)	10.38
^{74}Ge	^{74}Ni(^{3}He, ^{3}He γ)	-

Table 2.2: Reactions studied at OCL and the corresponding Q-values.

charged particle per unit length in a medium is a function of the mass and charge of the penetrating particle, according to the Bethe-Block formula [94]. The penetration depth in the material, as a function of the kinetic energy of the particle differs for each charged particle due to their different charge and mass. Identifying the particle of interest, in this case ^{3}He and α particles, ejectiles from the inelastic scattering and the neutron pick-up reaction are obtained by applying appropriate 2-D gates on the $\Delta E - E$ matrices. A plot of the energy deposited in the ΔE detector versus the energy deposited in the E detector is shown in Fig. 2.6.

From the kinematics of the reactions and the various Q-values the energy deposited in the particle telescopes was translated into initial excitation energy of the residual nuclei. The particle-γ coincidence data obtained are analysed by the Oslo method presented in the next chapter.

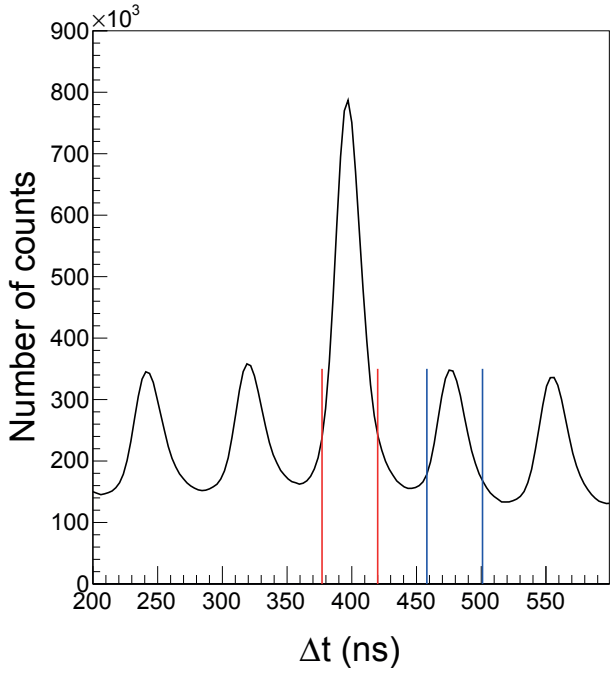

Figure 2.5: *A typical time spectrum showing the time difference between detection of a particle in the E back detector, and detection of a γ ray in the NaI detector. A set delay in the signal from the γ detection gives a time difference, Δt = 400 ns that is equivalent to a simultaneous detection of a particle and a γ ray. Red and blue lines indicate the gates set on the prompt peak and random peak, respectively, to subtract background events.*

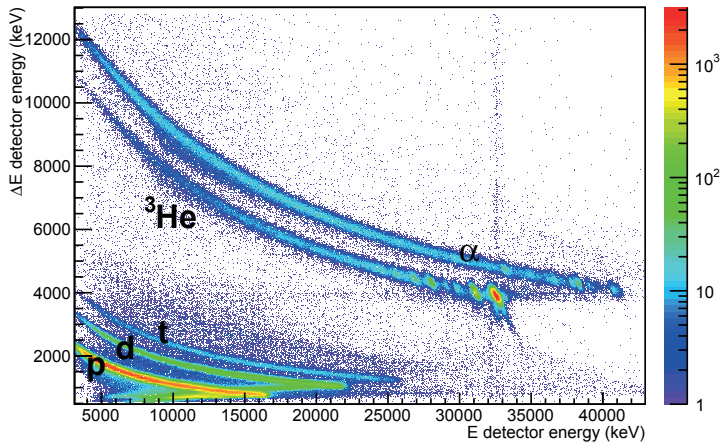

Figure 2.6: *Particle spectra from the ^{60}Ni + ^{3}He experiment, with the energy deposited in the thick E detector versus the thin ΔE detector, for $\theta = 42 \pm 1^\circ$.*

2.2 β-decay experiments

The experiment was performed at the National Superconducting Cyclotron Laboratory (NSCL) Coupled Cyclotron Facility (CCF) at Michigan State University. This facility is capable of producing a wide range of radioactive beams, using a fast in-flight fragmentation technique. An overview of the accelerator and the experimental areas is shown in Fig. 2.7. The two coupled cyclotrons at NSCL, an injector (K500) and a booster (K1200), are the heart of the facility. The beam-delivery process starts with an electron-cyclotron resonance (ERC) ion source. Stable positive ions are produced in the ERC source and injected directly in the first cyclotron (K500), where they are accelerated to $\approx$ 14 MeV/u. The advantage of the CCF is that the K500 provides the first stage of the acceleration. In this way, the injected ions are not required to be in a high charge state, resulting in higher output intensities from the ERC source and a higher intensity of the final beam. The accelerated ions are further injected into the K1200 and stripped of their remaining electrons by a carbon foil, before they are accelerated to an energy of typically $\approx$ 140 MeV/u. The beam is extracted using a high-voltage deflector to form the primary beam. A production target, typically of beryllium, is situated close to the the extraction line. The primary beam is impinging on this target, and the collision with the target nuclei results in the stochastic production of isotopes via fragmentation. The desired beam of radioactive nuclei is selected from the distribution of produced isotopes using the A1900 projectile-fragment separator [95] and delivered as a secondary beam to the various experimental areas.

In the present experiment, a primary beam of ^{76}Ge was accelerated to the energy of 130 MeV/u, and impinged on a Be ($\approx$ 500 mg/cm^2) production target. A secondary, slightly neutron rich, ^{76}Ga beam was produced in a fragmentation process. Since we are not interested in studying collisions, but rather the β-decay from Ga nuclei, the secondary beam needs to be stopped at this point. This was done by thermalization in a gas stopper, see Fig. 2.7 and for details see Ref. [97]. The thermalized beam was extracted and delivered to the experiment with an intensity of $\approx$ 500 pps.

2.2.1 Detector set up

Two detectors were utilized in the current experiment: a small silicon surface barrier detector and a Summing NaI (SuN) detector [98]. SuN is a large volume γ-ray total absorption spectrometer, shaped like a cylinder 16$''$ in length and 16$''$ in diameter. SuN is segmented in eight optically isolated segments, which can be used to observe individual γ transitions. Each segment is connected to three photo multipliertubes (PMT). The detector has in total a detection efficiency of $\approx$85% for individual γ rays with E$_\gamma$ = 661 keV. The signals from the individual 8

segments can be summed, in order to give a measure of the total γ energy emitted following β decay. A crucial part of the γ summing technique is the determination of the summing efficiency ε_Σ of SuN. This efficiency depends on both the sum-peak energy and the average multiplicity $\langle M \rangle$ of the decay cascade. For the summing of the two sequential γ-rays from the decay of ^{60}Co the sum-peak efficiency is $\approx$65%. However, in general the level scheme of the decaying nucleus is not known, and it becomes impossible to determine the quantity $\langle M \rangle$ exactly. A method is devised, based on the fact that the number of segments in SuN that fires in connection with an event increases with the number of γs in the cascade. Thus, the centroid of the hit pattern $\langle N_S \rangle$ will move towards higher energies. The summing efficiency of the SuN detector as a function of $\langle N_S \rangle$ is shown in Fig. 2.8. In our type of experiments, relatively low-spin states are populated in the β decay, leading to few de-excitation steps down to the ground state, corresponding to a multiplicity in the order of 2.5-3.5. This ensures a quite high total absorption efficiency of SuN.

A borehole of diameter 45 mm extends throughout the SuN detector parallel with its axis, see Fig. 2.9, and allows for placing a tiny particle detector in the geometrical center of SuN. During the experiment, a silicon surface barrier detector was placed in the center of SuN, and the ^{76}Ga beam was implanted in the detector. Because of the low beam energy ($\approx$ 30 keV), the beam particles were stopped in

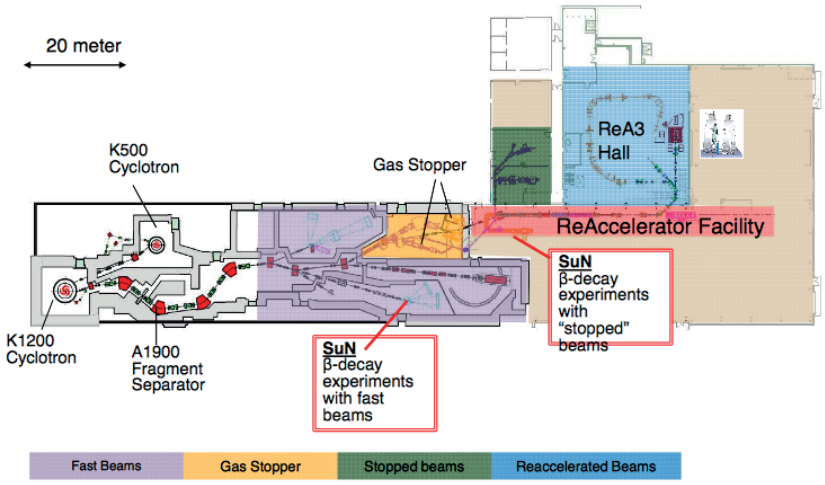

Figure 2.7: *The facility at NSCL. The figure taken from [96].*

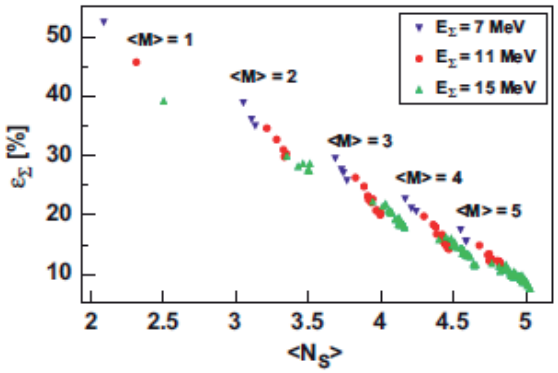

Figure 2.8: *Summing efficiency of the SuN detector as a function of the average number of hits $\langle N_S \rangle$ for various sum-peak energies. The figure is taken from [98].*

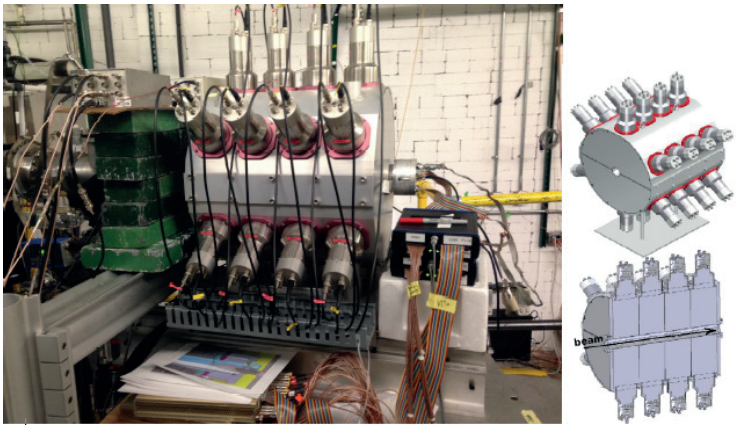

Figure 2.9: *The SuN detector. The drawings (from [98]) show the segments and the borehole.*

the dead layer in the silicon detector and did not provide a measurable signal. Due to the fact that there were no isotopic impurities, it was not imperative to retrieve any timing information from when the ^{76}Ga nuclei were implanted in the silicon detector.

2.2.2 Coincidence measurements

The radioactive isotope ^{76}Ga has a half-life $t_{1/2}$ = 32.6 s, and decays sending out β-particles ;

$$^{76}\text{Ga} \rightarrow ^{76}\text{Ge} + e^- + \bar{\nu}_e. \tag{2.1}$$

Directly following the β decay, the daughter nucleus, ^{76}Ge, will be in a state with excitation energy between 0 and 6.9 MeV (limited by the Q-value (6.9 MeV) of the reaction). Beta particles were detected in the silicon surface barrier detector in coincidence with γ rays in SuN. All signals were processed with the NSCL digital data acquisition system [99]. The raw coincidence matrix (E_γ, E_x) from the SuN detector is constructed, and the excitation energy is given by the total absorption spectrum,

$$E_x = E_{\gamma 1} + E_{\gamma 2} + ... + E_{\gamma M}, \tag{2.2}$$

where M is the multiplicity of the γ decay. If one or more γ rays from a cascade escapes the 4π γ detector, the resulting initial excitation energy of the nucleus of interest becomes incorrect. This source of uncertainty, called incomplete summing, needs to be investigated further. The individual segments in SuN provided the γ-ray energy E_γ of a random γ ray for the decay cascade. The coincidence

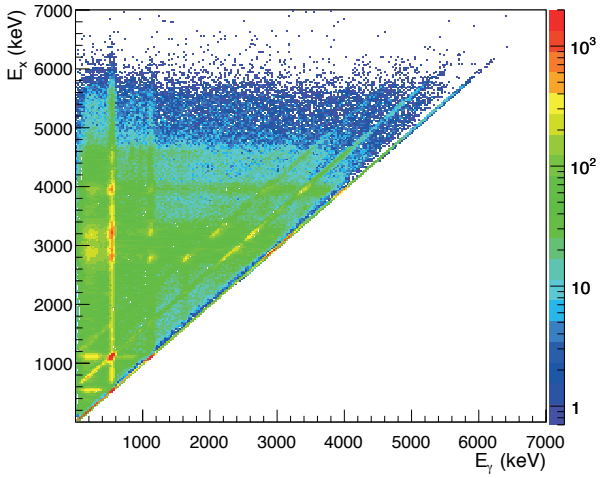

Figure 2.10: *The coincidence matrix of ^{76}Ge. The figure is taken from Ref. [100].*

matrix, (E_γ,E_x), is presented in Fig. 3.8. We observe a clear diagonal along E_x

= E_γ in the matrix, where the populated states in the β-reaction decay directly to the ground state. Also, we see direct decay to the first and second excited state of spin/parity 2^+. The particle-γ coincidence data obtained are analysed further by the Oslo method presented in the next chapter.

2.3 The photoneutron experiments

The photoneutron experiments were performed at the NewSUBARU laboratory [101], located at the SPring-8 site managed by RIKEN. Photoneutron measurements in the vicinity of S_n were performed on five Nd isotopes: $^{143-146,148}$Nd, seven stable Sm isotopes: $^{144,147-150,152,154}$Sm and one germanium isotope: ^{74}Ge. The two experiments were performed in 2013, and were the first (γ,n) experiments performed at the NewSUBARU facility after the research activity was moved from AIST Electron Accelerator Facility in 2012. The NewSUBARU radiation facility provides tunable almost monochromatic, γ-ray beams in a wide range of energies, providing excellent conditions for (γ,n) cross section measurements. At the SPring-8 facility, electrons are accelerated in a linear accelerator and injected into the NewSUBARU storage ring, as depicted in the schematic overview given in Fig. 2.11. The electrons are injected with an energy of 974 MeV and are subsequently accelerated or decelerated to energies in the range 0.5-1.5 GeV [101]. In our experiments, electron energies in the interval $\approx$ 600-900 MeV were used to increase the frequency of laser photons up to a desired energy in the MeV domain. The electron beam intensity varied from 200 to 65 mA, decreasing by approximately 12-13 mA per hour after the injection from the linac.

2.3.1 Production of the γ beam

The γ-ray beams used in the photoneutron experiments were produced in Laser Compton Scattering (LCS) by colliding the high-energy electrons circulating in the storage ring with laser photons.

The LCS plays the role of a photon-accelerator, and the energy of the resulting γ-rays is expressed by

$$E_\gamma = \frac{4\gamma^2 E_L}{1+(\gamma\theta)^2+4\gamma E_L/mc^2}, \tag{2.3}$$

where E_L is the energy of a laser photon, mc^2 is the rest mass energy of an electron, θ is the scattering angle of a laser photon with respect to the incident direction of the electrons, and γ is the Lorentz factor for the electrons, $\gamma = E_e/mc^2$, defined by the total electron energy E_e and the rest mass energy. The γ energy is maximized for $\theta = 0$ (near head on collisions), as we see from Eq. (2.3). The energy amplification factor E_γ/E_L in these nearly head-on collisions is very large, in the order of $10^6 - 10^7$, for electrons with energies from several hundred MeV to a few GeV [102]. This means that an eV laser beam can be converted to an MeV γ-ray beam in LCS experiments.

For the purpose of the current experiments, laser photons were produced by a Q-switch Nd:YVO_4 laser (wavelength λ = 1064 nm; power = 40 W). The Nd

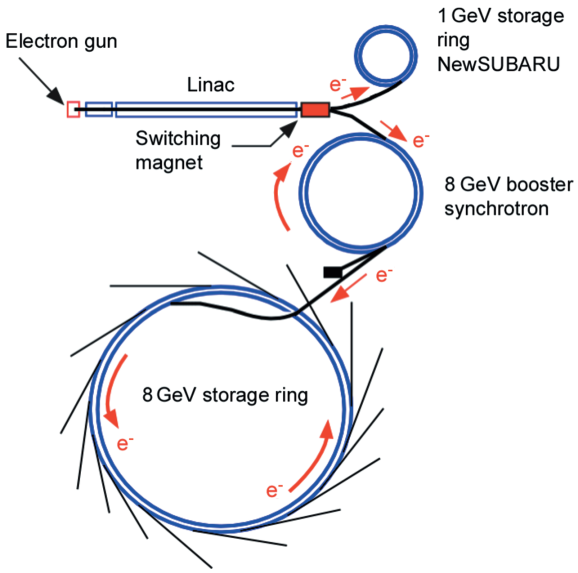

Figure 2.11: *A schematic overview of the accelerator complex at SPring-8 that is comprised of four accelerators: a 1-GeV linac, an 8-GeV booster synchrotron, an 8-GeV storage ring and the 1.5-GeV storage ring of NewSUBARU. The figure is taken from the homepage of SPring-8 [103].*

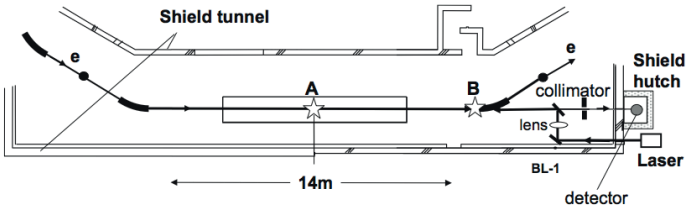

Figure 2.12: *An overview of the straight section of the storage ring, the two ideal collision points between the lasers and the electron beams, are marked with a star at position A and B.*

laser has a microscopic frequency of 20 kHz and a pulsed 10-Hz macroscopic time structure of 80 ms beam-on and 20 ms beam-off. At NewSUBARU a CO_2 laser (wavelength λ = 10.59 μm) is also accessible. It was used in the production of low-energy beams when performing a new energy calibration of the electron beam as a part of these experiments [102].

The collision points between the laser photons and the electron beam are located along the 14 m straight part of the storage ring, as indicated in Fig. 2.12, where they are marked with *A* and *B* for the Nd and CO_2 laser respectively. The collision points are carefully chosen to lie where the electron beam has a minimal transverse profile, increasing the probability of interaction between the laser photons and the electrons.

2.3.2 Experimental setup

The photoneutron cross section $\sigma(E_\gamma)$ is defined as

$$\int_{S_n}^{E_{\mathrm{Max}}} n_\gamma(E_\gamma)\sigma(E_\gamma)dE_\gamma = \frac{N_n}{N_t N_\gamma \xi \varepsilon_n g}, \tag{2.4}$$

where N_n represents the number of neutrons produced, N_t gives the number of target nuclei per unit area, N_γ is the number of γ rays incident on target, ε_n represents the neutron detection efficiency, and finally $\xi = (1-e^{\mu t})/(\mu t)$ is a correction factor for self attenuation in the target. The factor g represents the fraction of γ flux above the neutron separation energy S_n. The normalized energy distribution of the γ-ray beam $n_\gamma(E_\gamma)$ is included. Even though the γ beams produced in experiments have a high resolution a certain spread is inevitable.

Extracting our quantity of interest, $\sigma(E_\gamma)$, from inside the integral in Eq. (2.4), is not straightforward. As a first approximation, the γ-energy distribution $n_\gamma(E_\gamma)$ was replaced with a delta function $\delta(E_\gamma - E_{\mathrm{av}})$. We obtain the following cross section in the monochromatic approximation,

$$\sigma^{\mathrm{mono}}(E_{\mathrm{av}}) = \frac{N_n}{N_t N_\gamma \xi \varepsilon_n g}, \tag{2.5}$$

where E_{av} is the average energy of the LCS γ-ray beam given by:

$$E_{\mathrm{av}} = \frac{\int_{S_n}^{E_{\mathrm{Max}}} E_\gamma n_\gamma(E_\gamma)dE_\gamma}{\int_{S_n}^{E_{\mathrm{Max}}} n_\gamma(E_\gamma)dE_\gamma}. \tag{2.6}$$

The measurements were performed inside the beam line named GACKO, which is an acronym for GAmma Collaboration hutch of KOnan University. The different detectors were placed as depicted in Fig. 2.13. The target samples were situated

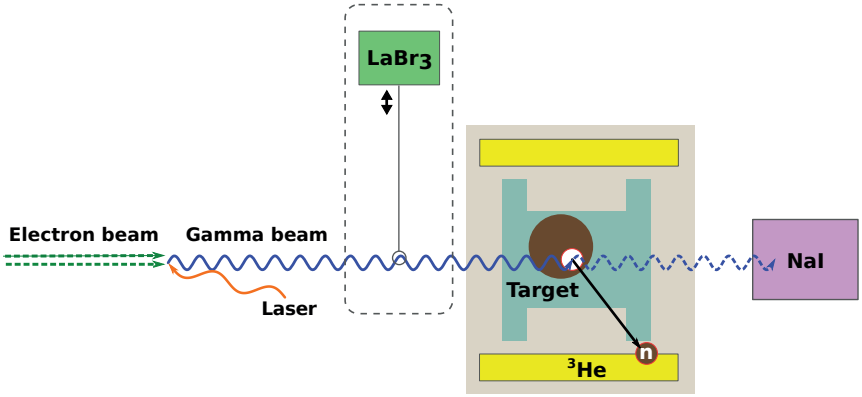

Figure 2.13: *A schematic drawing of the experimental setup and the collision point.*

inside aluminum containers (see Fig. 2.14). The neutron threshold for aluminum is $S_n = 13.1$ MeV, and to avoid opening the $\mathrm{Al}(\gamma, \mathrm{n})$ channel, the maximum energy of the γ beam was kept below 13 MeV. The measurements were carried out at $6-17$ different γ beam energies, depending on the target, ranging from the neutron separation energy of the target up to ≈ 13 MeV.

The process of measuring a (γ, n) cross section entails careful counting of the following quantities for each individual LCS γ-beam impinging on the target:

(i) The number of neutrons, N_n, which was measured with a ^{3}He-proportional counters.

(ii) The number of γ rays, N_γ, which was measured with a large NaI:Tl (NaI) detector at the end of the beam line.

The number of target nuclei, N_t, was established by a careful weighing of the aluminum containers with and without the target material inside. The beam energy profile, $n_\gamma(E_\gamma)$, was determined by inserting a $LaBr_3$ detector in the beam line at the beginning and the end of each run.

In the next sections a detailed description will be given of how the quantities of Eqs. (2.4) and (2.5) are measured and simulated.

2.3.3 Energy distribution of the γ-ray beam

A large volume Lanthanum Bromide ($LaBr_3$:Ce) detector, $3.5'' \times 4''$, was placed in the beam line to monitor the γ-ray beam profile before and after each run of

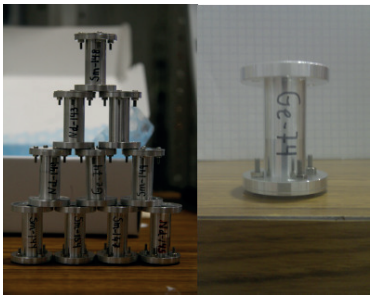

Figure 2.14: *The targets used in the measurements: ∼ 1-2 g of Nd and Sm oxides and ^{74}Ge in metal form, placed inside holders made of Al.*

a specific γ energy (see Fig. 2.13 and the right panel of Fig. 2.15). During these measurements, the laser operated in a continuous wave mode at reduced power, to lower the rate of produced LCS γ-rays, and thereby avoid pile-up effects. The resolution of the $LaBr_3$ detector was calibrated using γ transitions for ^{60}Co and ^{137}Cs sources, and was shown to be better than 2% for γ energies above 2.5 MeV. A GEANT4 code [104, 105], developed in connection with the current experiments, was used to simulate the collision between the relativistic electrons and the laser photons, the passage of the produced γ beam through collimators, and finally the detection in the $LaBr_3$ detector. In the left panel of Fig. 2.15, a typical simulated response spectrum of the $LaBr_3$ detector for a given incoming beam is shown. A more detailed description of the GEANT4 simulation is given in Article V and in Ref. [106]. The energy spreads (FWHM) of the incoming γ-ray beams were determined to be in the range of 1-2%.

2.3.4 Determining the γ-ray flux

The number of incident γ rays on the target, N_t, is a challenging entity to measure directly. We have chosen a well-proven method called the "pile-up method" [107] for this purpose. Due to the frequency of the Nd laser, λ = 20 kHz, bunches of photons and electrons collide every 5 μs inside the storage ring. Because of the extremely low probability of photons and electrons interacting, only a few, 1-3 (if any), LCS γ rays are produced per collision. If the produced LSC γ rays are not removed in collimators or interact with the target, they will impinge on the large-volume $5'' \times 6''$ NaI:Tl detector situated at the end of the beam line (see Fig. 2.13). LCS γ rays from the same collision will be detected as one signal in the NaI detector, as a usually unwanted pile-up event. As an example, a bunch of

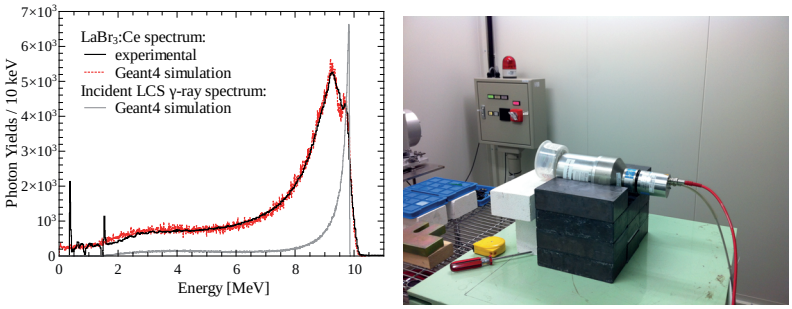

Figure 2.15: *Left panel: A typical $LaBr_3$ spectrum compared to the GEANT4 simulation and the unfolded spectrum. Right panel: The $LaBr_3$ detector placed along the beam line.*

three LSC γ rays detected simultaneously in the NaI detector will produce a single signal three times as big as a single LSC γ would give (due to the linearity of the NaI detector). The time intervals between the bunches of LCS γ rays (5 μs) is long enough for the NaI to interpret the bunches as separate events. Per individual run, a pile-up spectrum is recorded, as shown in Fig. 2.16. To be able to count the number of detected γ rays, we need a reference point in the form of the γ spectrum from only single γ events. This is accomplished by reducing the laser power to a point where the probability to boost more than one laser photon in a LCS event is negligible, giving a single γ spectrum as shown in the insert in Fig. 2.16.

From the pile-up and single spectra, we are able to deduce the number of detected γ-rays in the NaI detector:

$$N_{\gamma,\text{detected NaI}} = \frac{\langle i \rangle_{\text{pile up}}}{\langle i \rangle_{\text{single}}} (\sum n_i)_{\text{pile up}}, \tag{2.7}$$

where $\langle i \rangle = (\sum x_i n_i)/(\sum n_i)$ gives the average channel of the detected γ-rays for the pile-up and the single spectra, n_i being the number of counts in the i'th cannnel, x_i. The ratio of $\langle i \rangle$'s in Eq. (2.7) gives the average number of γs produced in each detected LCS bunch, while the sum of pile-up events, $(\sum n_i)_{\text{pile up}}$, gives the number of bunches having reached the detector.

The targets used in these experiments have to be quite thick, ~ 2 g/cm^2, due to the low probability of interaction between γ-rays and matter. Attenuation in the target has to be taken into account, giving the following expression for the total

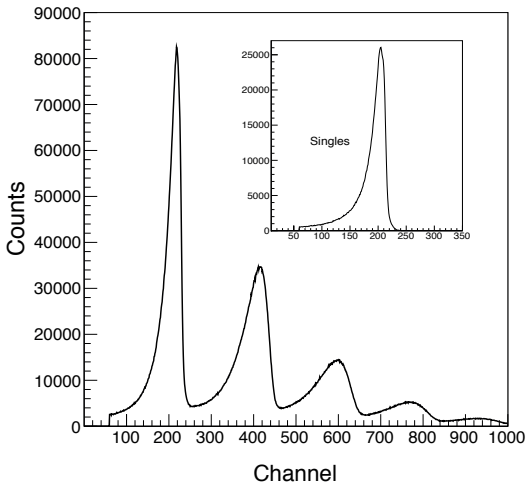

Figure 2.16: *A typical pile-up spectrum of the LCS γ-ray beam obtained with the* $6'' \times 5''$ *Na(Tl) detector. A single-photon spectrum is shown in the inset.*

number of γ rays detected:

$$N_{\gamma,\text{after target}} = N_{\gamma} \cdot \exp\left(-\frac{\mu_{\text{t}}}{\rho_{\text{t}}} t_{\text{t}}\right), \tag{2.8}$$

where t_{t} gives the target thickness, and $\frac{\mu_{\text{t}}}{\rho_{\text{t}}}$ represents the mass attenuation coefficient, tabulated in Ref. [108]. All of the target nuclei, except ^{74}Ge, were made of oxide material, in general the attenuation of a compound is given by

$$\frac{\mu}{\rho} = \sum_i w_i \frac{\mu_i}{\rho_i}, \tag{2.9}$$

where the summation is over the constituents of the compound, and w_i gives the fraction of each constituent to the total amount.

Finally, we have to take into consideration the fraction of the incoming γ rays not interacting with the detector. The following expression gives the number of γ rays on the target:

$$N_{\gamma,\text{detected NaI}} = N_{\gamma,\text{after target}} \cdot \left(1 - \exp\left(-\frac{\mu_{\text{NaI}}}{\rho_{\text{NaI}}} t_{\text{NaI}}\right)\right), \tag{2.10}$$

which results in the following expression for the total number of γ rays incident on the target:

$$N_\gamma = \frac{N_{\gamma,\text{detected NaI}}}{\exp\left(-\frac{\mu_t}{\rho_t}t_t\right)\left(1-\exp\left(-\frac{\mu_{NaI}}{\rho_{NaI}}t_{NaI}\right)\right)}. \quad (2.11)$$

Background subtraction was performed, using the macroscopic time structure of the Nd laser, subtracting the γ spectrum recorded in the 20 ms the laser is off per 100 ms. The uncertainty in the determination of the γ-ray flux is estimated to be $\sim$ 3 %, and is mainly due to the energy lack of linearity in response to multiphotons [109].

2.3.5 Neutron detection

The counting of emitted neutrons in the (γ,n) reactions was performed with a high efficiency 4π neutron detector comprised of 20 tubes of ^{3}He gas. The ^{3}He counters are arranged in a geometry of three concentric rings. The inner ring consist of four detectors and the two outer rings are comprised of eight detectors each. The counters are located at distances 3.8, 7.0 and 10.0 cm from the γ-ray beam axis, all embedded in a polyethylene box of dimension $36\times36\times50$ cm^3, as shown in Fig. 2.17. For background neutron suppression, 5 cm thick polyethylene plates with a 1 mm thick cadmium metal sheet were placed on each side of the box. The plastic box moderates the fast neutrons of maximum energy $\approx$ 7 MeV emitted form the target nuclei. The targets are situated in the center of the ^{3}He rings, inside a borehole in the polyethylene box. The ^{3}He gas efficiently detects thermal neutrons, through the reaction: ^{3}He + n $\rightarrow$ ^{4}He$^*\rightarrow$ ^{3}H + p, where the Q value of 764 keV leads to oppositely directed reaction products. The thermal neutron cross section for this reaction is 5330 barns. The background component was subtracted from the reaction and background neutrons using the 100 Hz frequency pulsed time structure of the incident LCS gamma-ray beam. Reaction neutrons and background neutrons are detected in the 80 ms when the Nd laser is on (N_n(on)) per 100 ms, and background neutrons are detected in the resulting 20 ms when the laser is off (N_n(off)).

The number of neutrons for each run is calculated as follows:

$$N = N_n(\text{on}) - 4\cdot N_n(\text{off}). \quad (2.12)$$

A few measurements for incoming γ beam energies below the neutron separation energies of the individual targets are performed, to confirm that the number of detected neutrons are ≈ 0.

We assume the following statistical uncertainty for when the beam is on and

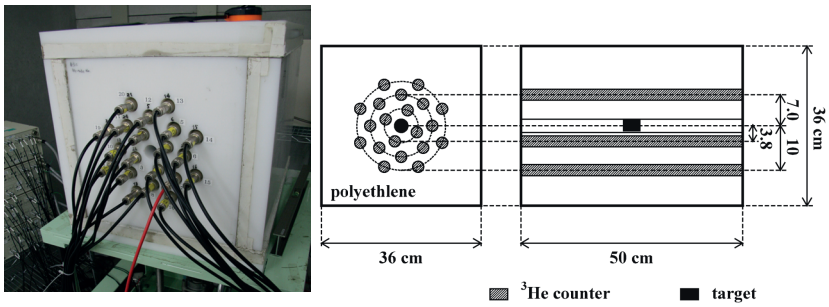

Figure 2.17: *Left panel: a photo of the moderator box and the end point of the 20 ^{3}He proportional counters placed in three concentric rings. Right panel: a schematic view of the target position and the ^{3}He detectors.*

off:

$$\Delta N_n(\text{on}) = \sqrt{N_n(\text{on})}, \tag{2.13}$$
$$\Delta N_n(\text{off}) = \sqrt{N_n(\text{off})}.$$

The total uncertainty in the number of neutrons is then

$$\Delta N_n^2 = \Delta N_n^2(\text{on}) + 16 \cdot \Delta N_n^2(\text{off}), \tag{2.14}$$
$$\Delta N_n^2 = N_n(\text{on}) + 16 \cdot N_n(\text{off}). \tag{2.15}$$

2.3.6 Efficiency of neutron detection

The triple-ring neutron detector with ^{3}He proportional counters is designed to achieve a high total efficiency of detecting neutrons in the energy range below 1 MeV with a capability of deducing the average neutron energy by the so-called ring ratio technique. This technique which was originally developed by Berman et al., [110], gives the average neutron energy as function of γ-ray beam average energy. Because the amount of moderator material between the neutron emission point and the three rings of neutron detectors is different, the individual rings of detectors have different detection efficiencies for neutrons with equal energy. We know how the average neutron energy depends on the ring ratio, and we are able to infer this energy, as shown in the upper panel of Fig. 2.18.

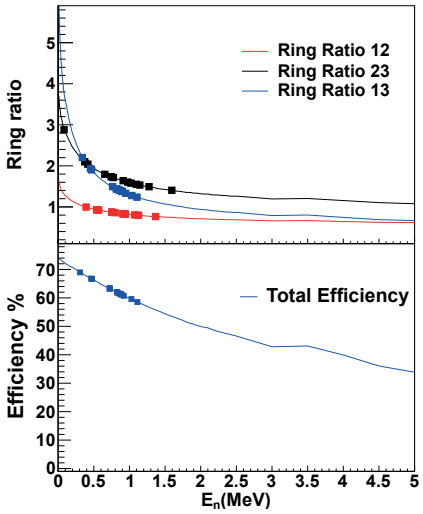

Figure 2.18: *Upper panel: measured ring ratios and the corresponding average neutron energy. Lower panel: the relation between the average neutron energy and the total efficiency of the* ^{3}*He counters. The solid lines represent MCNP Monte Carlo simulations, while the squares give values deduced form the measurements.*

We start by calculating the number of neutrons from each ring and the corresponding uncertainty from Eqs. (2.12) and (2.15). The ring ratios are given by:

$$\begin{aligned} R_{12} &= N_n^{r1}/N_n^{r2} \\ R_{23} &= N_n^{r2}/N_n^{r3} \\ R_{13} &= N_n^{r1}/N_n^{r3}, \end{aligned} \tag{2.16}$$

where the subscripts 1, 2 and 3 gives the ring number. The uncertainty of the ring ratios ΔR are calculated from error propagation,

$$\left(\frac{\Delta R_{12}}{R_{12}}\right)^2 = \left(\frac{\Delta N_n^{r1}}{N_n^{r1}}\right)^2 + \left(\frac{\Delta N_n^{r2}}{N_n^{r2}}\right)^2, \tag{2.17}$$

$$\Delta R_{12} = \sqrt{\left(\frac{\Delta N_n^{r1}}{N_n^{r1}}\right)^2 + \left(\frac{\Delta N_n^{r2}}{N_n^{r2}}\right)^2} \cdot R_{12}. \tag{2.18}$$

We know how the average neutron energy depends on the ring ratio, therefore we obtain energies E_{12}, E_{23} and E_{13} for each of the ring ratios. We find the uncer-

tainty of the energies from the uncertainty to the ring ratios, by simply adding and subtracting ΔR from R, and reading out the corresponding energy. The largest difference of these energies with respect to the energy calculated from R is assumed to be the uncertainty of the energy ΔE. Furthermore, we calculate the weighted average of the energies as follows,

$$E_n = \frac{\omega_{12}E_{12} + \omega_{23}E_{23} + \omega_{13}E_{13}}{\omega_{12} + \omega_{23} + \omega_{13}}, \tag{2.19}$$

where $\omega = 1/\Delta E$, for each of the rings. Once the energy is obtained one finds the corresponding efficiency from the simulations described in Ref. [111]. The total detection efficiency of the composite neutron detector as a function of average neutron energy is inferred from a MCNP Monte Carlo simulation, presented in the lower panel of Fig. 2.18. Neutron detection efficiencies of the three rings were measured after the experiments by using a calibrated ^{252}Cf source at the National Metrology Institute of Japan. The measurements were in excellent agreement with the simulations. According to Ref. [111], the uncertainty of the neutron detection efficiency is found to be 3.2% of the absolute emission rate of a ^{252}Cf source. This uncertainty is assumed in the analysis of the data presented in this work.

2.3.7 The monochromatic cross section

After a careful determination of all the entities of Eq. (2.5), the monochromatic cross sections can be deduced. In Fig. 2.19 the monochromatic cross section of ^{147}Sm is shown. The further processing technique of the data used to extract the non-monochromatic cross sections and finally deduce the inverse (n,γ) cross sections is presented in the next chapter.

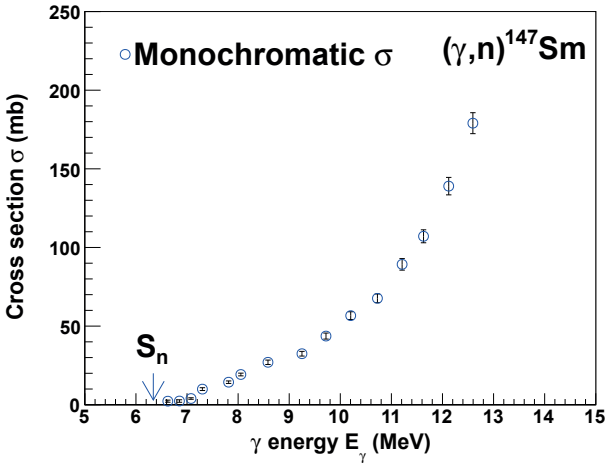

Figure 2.19: *The monochromatic (γ, n) cross section of ^{147}Sm.*

Chapter 3

Methods

In this chapter a brief description of the three methods used in in connection with this dissertation; the Oslo method, the β-Oslo method and the γSF method, are presented. The traditional Oslo method and the β-Oslo method are presented in parallel, since they are very similar.

3.1 The Oslo method

The Oslo method relies on four main steps: (i) the unfolding of the γ-ray spectra for each initial excitation energy; (ii) isolation of the primary γ-ray spectra, i.e., the distribution of the first emitted γ rays in all the γ-decay cascades for each initial excitation energy; (iii) extraction of the functional form of the NLD and the γ-ray transmission coefficient form the primary γ-ray spectra; (iv) normalisation of the NLD and the γSF. Experimental coincidence matrices obtained from the experiments performed at OCL and NSCL (see Chap. 2) have been analyzed in the framework of the Oslo method. The level densities and γSF below S_n have been extracted for ^{59,60}Ni and ^{73,74,76}Ge.

3.2 Unfolding the γ spectra

In the cases where incoming γ rays interact with the detector material of the γ detector, three processes are dominating: photoelectric effect, Compton scattering and pair production. In the ideal case, the incoming γ ray is completely absorbed in the detector material and found in the full-energy peak of the obtained γ-ray spectrum. Unfortunately, incidents where the incoming γ-ray deposits parts of its energy in the detector are very frequent. Compton scattered photons and one or both of the annihilation photons can escape the detector thus depositing only a part of its full energy. Additional background from backscattered annihilation

and Compton γ rays in the surroundings of the experimental setup produces peak structures at 511 keV and $\approx$ 200 keV, respectively.

The ratio between full-energy detection and partially detected γ-rays is often as low as $< 50\%$ [112]. A folding iteration method is therefore used to convert the detected γ-ray spectrum into the true spectrum. This method requires a knowledge of how the detector responds to γ rays in a wide energy range. The response function $R(E, E_\gamma)$ gives the relation between the energy E deposited in the detector and the energy E_γ of the incoming γ ray. The response function of the CACTUS array at OCL [92] have been measured for several in-beam γ lines from excited states in ^{13}C, ^{16,17}O, ^{28}Si and ^{56,57}Fe, where also the relative detector efficiency as function of γ energy could be extracted in a reliable way [113]. The response functions for the segments of the SuN detector at NSCL has been generated with the GEANT4 simulation tool and validated using standard radioactive sources and known resonances.

An interpolation procedure described in Ref. [112] is used between the measured discrete γ energies in order to obtain the response function for all γ energies. The unfolding procedure is described in Ref. [112], but since the response functions and detector efficiencies of the CACTUS array recently have been remeasured, the information Table 1 of Ref. [112] is outdated, and should be replaced with the values given in Appendix A.

A γ ray that is scattered at an angle θ transfers an energy E to the electron as given by

$$E_e = E_\gamma - \frac{E_\gamma}{1 + \frac{E_\gamma}{m_e c^2}(1 - \cos\theta)}, \tag{3.1}$$

where m_e is the rest mass of the electron and c represents the speed of light. When interpolating the Compton background, this is performed for channels with the same scattering angle (see Fig. 3.1).

The response functions are normalized by $\sum_i R_{ij} = 1$, where channel i represents the amount of energy deposited in the detector, when a γ ray of energy corresponding to channel j hits the detector. The folded spectrum f can be calculated a follows,

$$f = \mathbf{R}u, \tag{3.2}$$

where u represents the unfolded spectrum.

We use a folding iteration method [112] which consists of the following steps:

(i) We start with the observed raw spectrum r as a trial function for the unfolded spectrum u^0, $u^0 = r$.

(ii) The folded spectrum is calculated, $f^0 = \mathbf{R}u^0$.

(iii) For the next trial function, we add the difference $r - f^0$ to the original trial function u^0, $u^1 = u^0 + (r - f^0)$.

(iv) The next step entails a folding of u^1 to obtain f^1 which is again used to obtain the next trial function. The first three steps will be repeated until f^i reproduces r within the experimental fluctuations.

In order to achieve the best unfolding result with this method, the resolution (FWHM) of the response matrix used in the folding should be set to 10% of the resolution of the experimentally observed response functions.

3.2.1 The Compton subtraction method

A problem with the unfolding iteration method is that fluctuations in the spectra will increase and propagate for each iteration. To circumvent this problem, the Compton subtraction method has been developed. The essence of this method is to smooth the Compton contribution, before subtracting it from the observed spectrum. As a result an unfolded spectrum with the same fluctuations as the observed spectra, is obtained. The unfolded spectrum obtained from the folding iteration procedure serves as a starting point for the method. The observed spectrum, con-

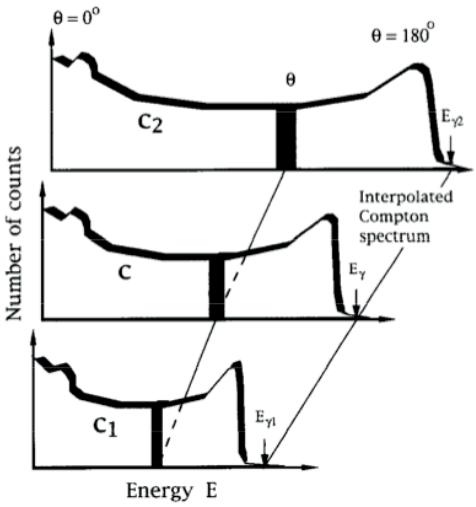

Figure 3.1: *Illustration of the interpolation of the Compton part of the measured response functions c_1 and c_2. The figure is taken from Ref. [112].*

taining all but the Compton contribution, is defined as [112],

$$v(i) = p_f(i)u_0(i) + w(i), \tag{3.3}$$

where the first term represents the full energy contribution, followed by $w(i) = u_s + u_d + u_a$, which gives the single- and double-escape peak and annihilation peak. These three terms are given by,

$$u_s(i - i_{511}) = p_s(i)u_0(i) \tag{3.4}$$
$$u_d(i - i_{1022}) = p_d(i)u_0(i) \tag{3.5}$$
$$u_a(i_{511}) = p_a(i)u_0(i). \tag{3.6}$$

The probabilities p_s, p_d and p_a which refer to the single- and double-escape peak and annihilation peak, are estimated from the measured monoenergetic transitions. To attain the energy resolution of the observed spectrum, the u_a spectrum is smoothed with an energy resolution of 1 FWHM. The energy resolution of u_s, u_d and u_a is determined from the observed spectrum (1 FWHM) and the response matrix (0.1 FWHM), namely $\sqrt{1^2 + 0.1^2}$ FWHM $= \sqrt{1.01} \approx 1$ FWHM.

After smoothening the spectra we extract the Compton background $c(i)$ from the observed spectra $r(i)$,

$$c(i) = r(i) - v(i). \tag{3.7}$$

The Compton contribution $c(i)$ should vary slowly as a function of energy. We can thus apply a strong smoothening to obtain a resolution of 1 FWHM. The smoothed Compton spectra and peak structures are then subtracted from the observed spectra, and the γ-ray energy distribution is corrected for full energy probability p_f and the detection efficiency ε_{tot} [112],

$$u(i) = \frac{r(i) - c(i) - w(i)}{p_f(i)\varepsilon_{\text{tot}}(i)}. \tag{3.8}$$

See Fig. 3.2 for examples of unfolded matrices from the ^{74}Ge and ^{76}Ge experiment, respectively.

Recently, the Compton subtraction method has been successfully used to obtain unfolded γ spectra with small fluctuations for γ-spectra recorded with $LaBr_3$ [81], and Ge detectors [114]. Furthermore, the unfolding procedure developed by the Oslo group has recently been successfully used by other nuclear physics groups [115].

3.2.2 First generation γ rays

The γ-decay from highly excited states consists in general of a cascade of γ-ray transitions. Unfortunately, the individual γ-ray transitions cannot be distinguished

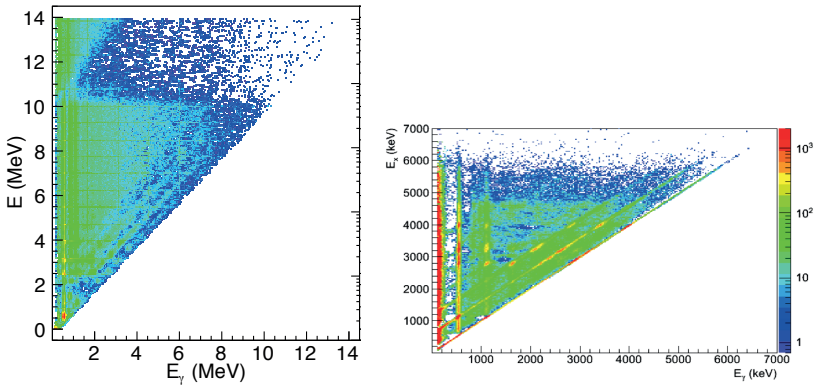

(a) *Unfolded* ^{74}*Ge.* (b) *Unfolded* ^{76}*Ge.*

Figure 3.2: *Unfolded coincidence matrices from (a) an experiment at OCL and (b) from the experiment at NSCL.*

because of the fast decay of these processes. As a consequence the measured γ-ray spectra will contain contributions from all generations of γ rays in the cascade. In order to investigate the transitions that originates from one specific excitation bin, it is necessary to extract information on the distribution of first γ-rays emitted in cascades starting from this specific excitation bin. The nuclear physics group at OCL has developed a method for this purpose. The method is described in detail in Ref. [116] but its main features will be explained here. We start with a simplified example to illustrate the idea behind the method. If we allowed ourselves to assume that each excitation bin had an equal chance of being populated in the reaction, we could find the primary γ-rays by subtracting the spectra from bins of lower excitation energy,

$$h_i = f_i - \sum_j w_{ij} f_j, \tag{3.9}$$

where h_i gives the primary γ rays at the initial excitation energy bin i, f denotes unfolded spectra, and w_{ij} is an unknown coefficient that gives the probability of decay from states in bin i to states in bin j. This factor is normalized such that $\sum_i w_{ij} = 1$, which gives the branching ratios as a function of excitation energy. In other words, w_i gives the primary γ ray spectrum h_i at bin i.

However, we know that the excitation levels populated in direct reactions are not randomly populated. E.g. reactions induced by ^{3}He particles, will have a large cross section for populating vibrational states with relatively high angular

momentum. To account for this we introduce a new factor n_{ij}, that when multiplied with each spectra f_i, gives the same number of cascades. Adding this to Eq. (3.9) we obtain the following expression for calculating the primary γ rays,

$$h_i = f_i - \sum_j w_{ij} n_{ij} f_j. \tag{3.10}$$

In the following two techniques we used to obtain the normalisation factor are presented.

- **Singles normalisation.** In order to account for the different cross sections of populating various energy bins, the singles particle spectrum can be employed. This spectrum provides the number of cascades decaying from this bin, as it is is proportional to the reaction yield. By dividing the number of counts S in the single particle spectra, the population of one level i relative to a level j is found,

$$n_{ij} = \frac{S_i}{S_j}. \tag{3.11}$$

- **Multiplicity normalisation.** The average γ ray multiplicity describes the average number of γ rays in the cascades. The average γ-ray energy $\langle E_{\gamma,i} \rangle$ decaying from a energy level i is expressed as follows,

$$\langle E_{\gamma,i} \rangle = \frac{E_i}{\langle M_i \rangle}, \tag{3.12}$$

  where E_i is equal to the total energy carried by the γ rays (equal to the excitation energy of the populated bin), and $\langle M_i \rangle$ is the average multiplicity from this level. A rearrangement of Eq. (3.12), provides the following expression for the multiplicity,

$$\langle M_i \rangle = \frac{E_i}{\langle E_{\gamma,i} \rangle}. \tag{3.13}$$

  Furthermore, the singles cross section S_i is equal to the area of spectrum f_i (the number of cascades), $A(f_i)$, divided by the multiplicity, $S_i = A(f_i)/\langle M_i \rangle$. By instering this into Eq. (3.11), we obtain,

$$n_{ij} = \frac{A(f_i)/\langle M_i \rangle}{A(f_j)/\langle M_j \rangle}. \tag{3.14}$$

The two normalisation methods have been thoroughly tested and compared in Ref. [43], where it was established that they normally rendered very similar results. One exception of this is when isomeric states are present. Then, the multiplicity method must be used to obtain the correct result.

The area of the primary γ-ray matrix should be equal to the area of the observed spectrum minus the area of the sum in Eq. (3.10), but this is not always the case because of an incorrect choice of the weighting function w. An area correction [116] is implemented to compensate for this,

$$A(h_i) = A(f_i) - \delta A(g_i), \tag{3.15}$$

where $g_i = \sum_0^j w_{ij} n_{ij} f_i$, and δ is a small correction. The same value can be expressed by,

$$A(h_i) = \frac{A(f_i)}{\langle M_i \rangle}. \tag{3.16}$$

When combining Eqs. (3.15,3.16), we obtain,

$$\delta = (1 - 1/\langle M_i \rangle) \frac{A(f_i)}{A(g_i)}. \tag{3.17}$$

To reach the best agreement between the areas of h_i, f_i and g_i, the correction parameter δ is varied. This correction is restricted to be maximum 15%.

3.2.3 Assumptions in the primary γ-ray method

The main assumption behind this method is that the γ-decay pattern from any excitation energy bin is independent of the population mechanism of states within the bin, e.g. direct population by a nuclear reaction, or population by a nuclear reaction followed by one or several γ rays (see Fig. 3.3) In the region of high level density, the nucleus seems to attain a compound-like system before emitting γ rays, even though direct reactions are utilized. This is due to a significant configuration mixing of the levels when the level spacing is comparable to the residual interaction. Because formation of a complete compound state is as fast as $\sim 10^{-18}$ s (which is significantly shorter than the typical life time of a state in the quasi-continuum which is $\sim 10^{-15}$ s) the compound nucleus condition is likely to be fulfilled. Therefore, the assumption is believed to be reasonable, and the decay process is in large statistical.

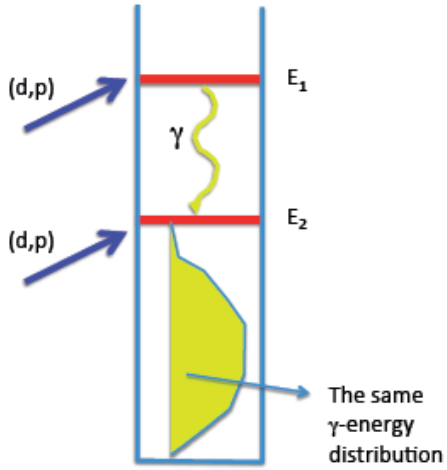

Figure 3.3: *The assumption of the extraction of primary spectra is that we obtain the same energy distribution (yellow) whether the levels of the energy bin E_2 are populated directly or by transitions from excitation bin E_1. The figure is taken from Ref. [121].*

3.2.4 The iteration procedure

Because w and the primary γ-ray spectrum h (see Eq. (3.9)) are identical, both can be determined through an iterative procedure [116]. To do this, we:

1. Apply a trial function for w_{ij}.

2. Deduce h_i.

3. Extract new w_{ij} functions from h_i by giving both variables the same energy calibration, and normalise the area of h_i to unity.

4. If $w_{ij}(\text{new}) \approx \text{w}_{\text{ij}}(\text{old})$, convergence is achieved: if not, repeat from step 2.

Since the resulting primary γ-ray spectra are not sensitive to the starting trial function [43], one could for example begin with the total unfolded spectrum. The procedure converges quickly, normally within $10-20$ iterations [43].

The primary γ-ray matrix of ^{74}Ge is shown in Fig. 3.4.

3.2.5 Extraction of level density and γ-ray strength function

At this stage of the Oslo method we have obtained a matrix of deduced distributions of primary γ-rays as a function of excitation bin. The information is stored in a matrix denoted P(E_γ,E), where E_γ and E are the γ energy and excitation energy respectively. The Oslo method enables us to extract both the NLD and the γSF via a factorization of the first generation matrix P(E_γ,E) [117]. These functions are extracted below the neutron separation threshold for a relatively low spin region ($0-10\,\hbar$). For a detailed description of the method see Ref. [117].

According to Fermi's golden rule, the decay probability may be factorized into the transition matrix element between the initial and final states, and the density of final states [118]:

$$\lambda_{i\to f} = \frac{2\pi}{\hbar} |\langle f|H'|i\rangle|^2 \rho_f \tag{3.18}$$

The deduced primary γ ray spectra P(E_γ,E) is proportional to $\lambda_{i\to f}$. As a consequence, a simplified version of Fermi's golden rule is introduced:

$$P(E_\gamma, E) \propto \mathscr{T}(E_\gamma)\rho(E-E_\gamma), \tag{3.19}$$

where $\mathscr{T}(E_\gamma)$ is the γ-transmission coefficient and $\rho(E-E_\gamma)$ is the NLD at the excitation energy E-E_γ after the primary γ-ray transmission. The transition matrix element $|\langle f|H'|i\rangle|^2$ from Eq. (3.18) has been replaced with a γ-transmission

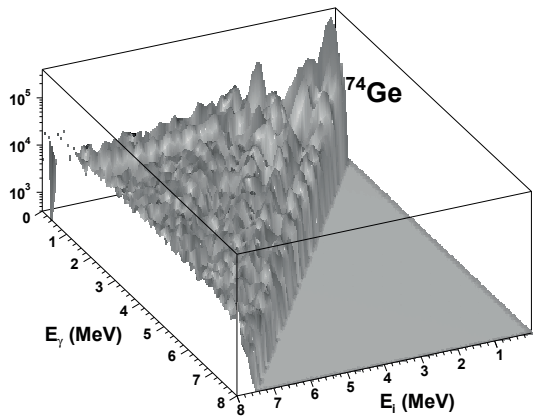

Figure 3.4: *The primary γ-ray distribution as a function of excitation energy.*

coefficient that, does not depend on initial and final excitation state, but solely on the size of the transitional γ ray. This simplification is in accordance with the generalized Brink hypothesis [119], stating that any collective decay modes have the same properties whether built on the ground states or on excited states. This assumption has been investigated in detail in Ref. [43], and has proven to be a good approximation for nuclei γ-decay in the quasi-continuum region for a wide range of nuclei.

Eq. (3.19) permits a factorization of the primary γ-ray matrix into two vectors, $\mathscr{T}(E_\gamma)$ and $\rho(E-E_\gamma)$. Since none of the two vectors are known in advance, a global iterative χ^2 minimisation is performed:

$$\chi^2 = \frac{1}{N} \sum_{E_i=E_i^{\min}}^{E_i^{\max}} \sum_{E_\gamma=E_\gamma^{\min}}^{E_i^{\max}} \left(\frac{P(E_i,E_\gamma) - P_{\exp}(E_i,E_\gamma)}{\Delta P(E_i,E_\gamma)} \right)^2, \tag{3.20}$$

where $\Delta P(E_i,E_\gamma)$ is the uncertainty matrix for the experimental first generation γ-ray distribution and N represents the degrees of freedom, which is equal to

$$N = N_P - N_\rho - N_{\mathscr{T}} \tag{3.21}$$

where N_P is the number of entries in the primary γ ray matrix, and N_ρ and $N_{\mathscr{T}}$ are the numbers of data points in the vectors to be determined [117]. All the vector elements in $\mathscr{T}(E_\gamma)$ and $\rho(E-E_\gamma)$ are treated as free parameters in the iterative χ^2 minimisation. The number of data points in the first generation matrix, N_P, are approximately one order of magnitude larger than the free parameters that are varied to reproduce them.

The normalised primary γ-ray matrix can be written as

$$P(E_i,E_\gamma) = \frac{\mathscr{T}(E_\gamma)\rho(E_i-E_\gamma)}{\sum_{E_\gamma=E_\gamma^{\min}}^{E_i} \mathscr{T}(E_\gamma)\rho(E_i-E_\gamma)}. \tag{3.22}$$

In this global iteration technique, χ^2 is minimised with respect to $\mathscr{T}$ for every γ energy bin and with respect to ρ for every excitation energy $E_f = E_i - E_\gamma$,

$$\frac{\partial}{\partial \mathscr{T}(E_\gamma)}\chi^2 = 0 \quad \text{and} \quad \frac{\partial}{\partial \rho(E_i-E_\gamma)}\chi^2 = 0. \tag{3.23}$$

A clear strength of this method, is its complete model-independence. That is, no models are used for the initial ρ and $\mathscr{T}$ functions in the χ^2 minimisation. The zeroth order estimate of the functions can be chosen arbitrary. For the NLD $\rho^{(0)} = 1$ is chosen. Inserting this function into Eq. (3.22) we obtain

$$P(E_i,E_\gamma) = \frac{\mathscr{T}(^{(0)}E_\gamma)}{\sum_{E_\gamma=E_\gamma^{\min}}^{E_i}\mathscr{T}^{(0)}(E_\gamma)}. \tag{3.24}$$

A summation over all excitation energy bins is performed,

$$\sum_{E_i=\max(\mathrm{E_i^{min}},\mathrm{E}_\gamma)}^{E_i^{\max}} P(E_i,E_\gamma) = \mathscr{T}^{(0)}(E_\gamma) \sum_{E_i=\max(\mathrm{E_i^{min}},\mathrm{E}_\gamma)}^{E_i^{\max}} \frac{1}{\sum_{E_\gamma=E_\gamma^{\min}}^{E_i}\mathscr{T}^{(0)}(E_\gamma)}. \tag{3.25}$$

We choose to let the sum on the right hand side equal unity, thus obtaining the zeroth order estimate for $\mathscr{T}$,

$$\mathscr{T}^{(0)}(E_\gamma) = \sum_{\max(\mathrm{E_i^{min}},\mathrm{E}_\gamma)}^{E_i^{\max}} P(E_i,E_\gamma). \tag{3.26}$$

The next step is to calculate higher order estimates. To do so we have to evaluate Eq. (3.23), in doing so we can derive the following expressions [117],

$$\mathscr{T}(E_\gamma) = \frac{\sum_{\max(\mathrm{E_i^{min}},\mathrm{E}_\gamma)}^{E_i^{\max}}\rho(E_i-E_\gamma)\phi(E_i,E_\gamma)}{\sum_{\max(\mathrm{E_i^{min}},\mathrm{E}_\gamma)}^{E_i^{\max}}\rho^2(E_i-E_\gamma)\psi(E_i,E_\gamma)} \tag{3.27}$$

$$\rho(E_f) = \frac{\sum_{\max(\mathrm{E_i^{min}},\mathrm{E_f}+\mathrm{E_\gamma^{min}})}^{E_i^{\max}}\mathscr{T}(E_i-E_f)\phi(E_i,E_i-E_f)}{\sum_{\max(\mathrm{E_i^{min}},\mathrm{E_f}+\mathrm{E_\gamma^{min}})}^{E_i^{\max}}\mathscr{T}^2(E_i-E_f)\psi(E_i,E_i-E_f)}, \tag{3.28}$$

where

$$\phi(E_i,E_\gamma) = \frac{a(E_i)}{s^3(E_i)} - \frac{b(E_i)}{s^2(E_i)} + \frac{P(E_i,E_\gamma)}{s(E_i)(\Delta P(E_i,E_\gamma))^2} \tag{3.29}$$

$$\psi(E_i,E_\gamma) = \frac{1}{(s(E_i)\Delta P(E_i,E_\gamma))^2}, \tag{3.30}$$

and

$$a(E_i) = \sum_{E_\gamma=E_\gamma^{\min}} \left(\frac{\mathscr{T}(E_\gamma)\rho(E_i-E_\gamma)}{\Delta P(E_i,E_\gamma)}\right)^2 \tag{3.31}$$

$$b(E_i) = \sum_{E_\gamma=E_\gamma^{\min}} \frac{\mathscr{T}(E_\gamma)\rho(E_i-E_\gamma)P(E_i,E_\gamma)}{(\Delta P(E_i,E_\gamma))^2} \tag{3.32}$$

$$s(E_i) = \sum_{E_\gamma=E_\gamma^{\min}} \mathscr{T}(E_\gamma)\rho(E_i-E_\gamma). \tag{3.33}$$

For each new iteration, we calculate a, b and s, from Eqs. (3.31)-(3.33). The result is inserted into Eqs. (3.29) and (3.30) to obtain ϕ and ψ. Finally, new estimates of the functions ρ and $\mathscr{T}$ are given, using Eqs. (3.27) and (3.28). Shown in Fig. 3.5 is an illustration of how the summations used in the above equations are performed. When extracting ρ and $\mathscr{T}$, only the white region of the figures are used. Due to non-statistical γ decay, the low excitation energy region is excluded. Due to insufficient subtraction of yrast transitions and limitations in the electronics that renders the low γ-ray energy regions unreliable, they are excluded. We see from the left panel of Fig. 3.5 that the summation must begin from $E_i = E_\gamma$ when the γ energy E_γ exceeds the minimum excitation energy $E_{i,\mathrm{min}}$.

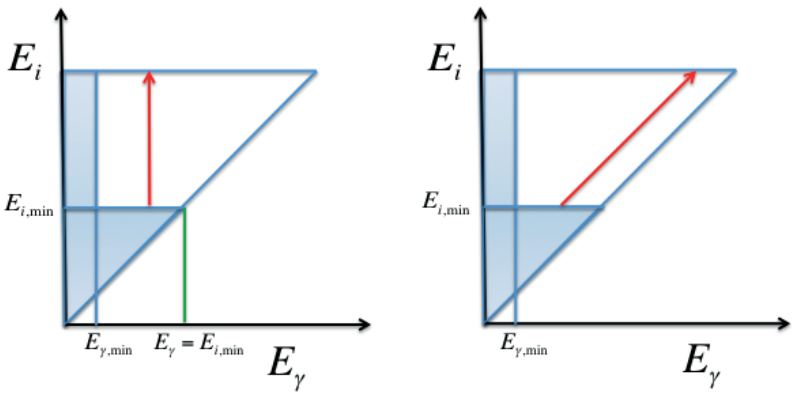

Figure 3.5: *An illustration of how the summation over the excitation energy bins (left), and γ energy bins (right) of the primary γ-ray matrix are performed. The red lines give the directions of the summation. The shaded area is usually excluded due to methodical problems.*

A χ^2 minimum is generally reached within 10-20 iterations. However, in some cases the χ^2-minimum is very shallow. To ensure that we actually find the global minimum a restriction to the maximum change of every datapoint of ρ and $\mathscr{T}$ within one iteration is set to a percentage P [117]. The quality of the extraction procedure can be inspected by comparing the primary γ-ray spectra calculated from the obtained ρ- and $\mathscr{T}$-functions with the experimental ones. This is a stringent test of how well the ρ- and $\mathscr{T}$-functions, which are found through a global fit of all the primary γ spectra within the fit region, can reproduce individual primary γ spectra from specific narrow energy regions. The first generation spectra P for ^{76}Ge at six different excitation energies are displayed in Fig. 3.6 and compared to

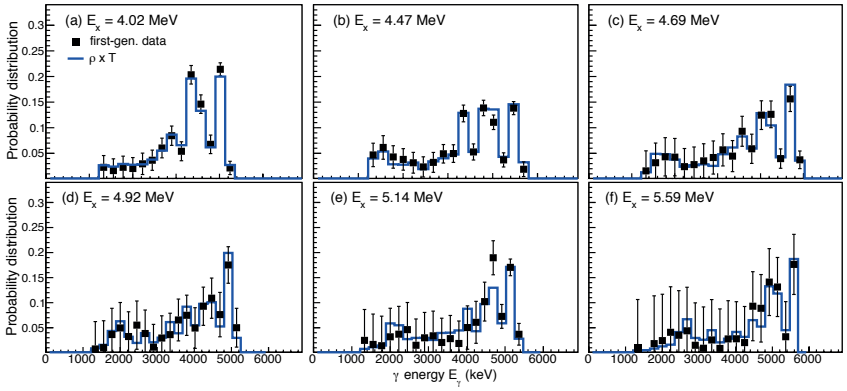

Figure 3.6: *Test of the extraction procedure to obtain the level density and γ-transmission coefficient. The experimental distributions of primary γ-rays for various excitation energies in the range E_x = 4.02-5.59 MeV (data points in panels (a) to (f)) are compared to the product $\rho(E-E_\gamma)\cdot\mathscr{T}(E_\gamma)$ (blue line) of the extracted NLD and γ-transmission coefficient. Excitation-energy bins are 224 keV wide. The figure is taken from the supplemental material of Paper II.*

the spectra obtained by multiplying the extracted ρ and $\mathscr{T}$ functions. In general, the agreement between the experimental data and the fit is very good. The small local deviations might be caused by large Porter-Thomas fluctuations [120] which are not taken into account in the extraction procedure.

3.2.6 Normalisation procedure

The functional form of ρ and $\mathscr{T}$ has been uniquely defined in the global-fit extraction. This means that structures in the ρ and $\mathscr{T}$ will not be changed from this point in the analysis. The only remaining challenge is the fact that our deduced functions do not represent the only solution of the factorization problem. Actually, one may construct an infinite number of other functions from the directly extracted solutions, which give identical fits to the $P(E_\gamma,E)$ matrix by applying the transformations [117]:

$$\tilde{\rho}(E-E_\gamma) = \mathrm{A}\exp[\alpha(E-E_\gamma)]\,\rho(E-E_\gamma), \tag{3.34}$$

$$\tilde{\mathscr{T}}(E_\gamma) = \mathrm{B}\exp(\alpha E_\gamma)\,\mathscr{T}(E_\gamma), \tag{3.35}$$

where A, B and α needs to be determined. These parameters cannot be deduced from information available from our experiments, so from this point in the analysis we depend on external data.

Normalising ρ

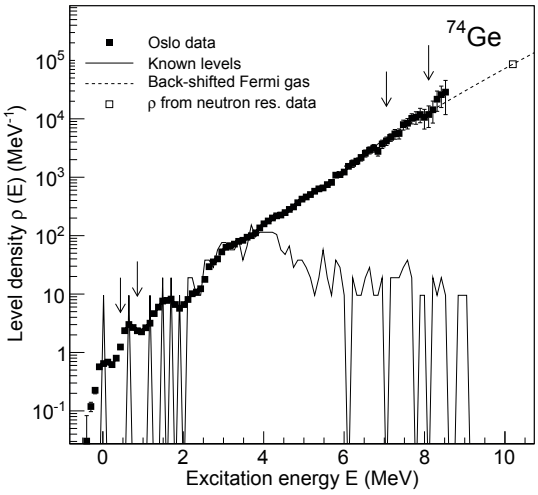

Figure 3.7: *The normalisation procedure for the experimental level density. The experimental data are normalized to known discrete levels at low excitation energy and to the level density extracted at S_n.*

For the NLD, the parameters α and A can be determined by using two anchor points. The procedure is demonstrated for the case of ^{74}Ge in Fig. 3.7. The NLD is normalized to known discrete levels at low excitation energies, and at high energies from the density of neutron resonances following (n,γ) capture at the neutron separation energy S_n. The NLD $\rho(S_n)$ can be estimated from s-wave (or p-wave) resonance spacings D_0 (or D_1) taken from RIPL-3 [44]. The total NLD at the neutron separation energy assuming s-wave ($l = 0$) is [117],

$$\rho(S_n) = \frac{2\sigma^2}{D_0}\frac{1}{(I+1)\exp[-(I+1)^2/2\sigma^2]+\exp[-I^2/2\sigma^2]}, \tag{3.36}$$

where I is the spin of the target nucleus. The spin-cutoff parameter, σ, entering this equation can be be parameterized as described in Chap. 2. The NLD at S_n can also be established from the microscopic calculations of [36], normalized to known resonance spacings. In Fig. 3.8, we display the resulting spin distributions at S_n obtained through the different approaches. Since the actual spin distribution is inaccessible in direct measurements, all three distributions should be used. The experimental data normally extends up to $\sim S_n - 1$ MeV, we therefore extrapolate $\rho(S_n)$ by a Fermi gas [117] or a constant-temperature level density [121] to fill the gap between the data and the calculated $\rho(S_n)$. An illustration of the normalisation of ρ is given in Fig. 3.7. A thorough description of the different approaches to determine $\rho(S_n)$ is given in Paper I.

Normalising $\mathscr{T}$

The only remaining unknown in Eqs. (3.34) and (3.35) is B, which scales the transmission coefficient $\mathscr{T}$. It is determined using the average total radiative width $\langle\Gamma_\gamma\rangle$ at S_n. Assuming that the γ decay is dominated by dipole transitions, the width is given by [122]

$$\langle\Gamma_\gamma\rangle = \frac{1}{2\pi\rho(S_n,I,\pi)}\sum_{I_f}\int_0^{S_n} dE_\gamma B\mathscr{T}(E_\gamma)\rho(S_n-E_\gamma,I_f), \qquad (3.37)$$

for initial spin I and parity π. The summation and integration run over all final levels with spin I_f that are accessible by $E1$ or $M1$ transitions with energy E_γ. From Eq. (3.37) we can extract B.

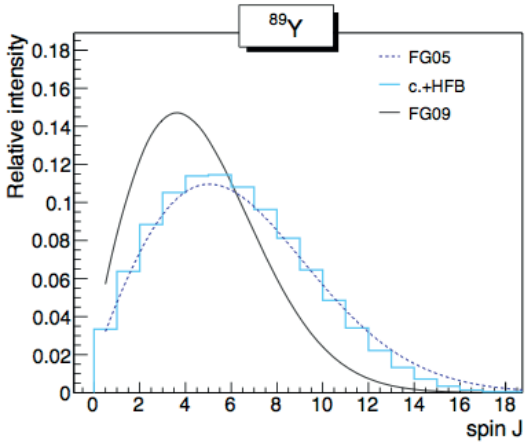

Figure 3.8: *Spin distribution of* ^{89}Y *at the neutron separation energy for two different parameterizations of the Fermi-gas model spin distribution (see Refs. [33, 34] and one from a Hartree-Fock-Bogoliubov plus combinatorial approach [36].*

3.3 The γ-ray strength function (γSF) method

The main purpose of the γSF method is to indirectly determine (n,γ) cross sections of radioactive nuclei. This method consists of three steps: (i) a series of high precision measurements of (γ,n) cross sections near S_n for stable isotopes of the radioactive element of interest; (ii) a deduction of the γSF from the measured (γ,n) cross sections and an extrapolation of the γSF to the energy region below S_n using Quasi-Random Phase Approximation (QRPA) models; (iii) reproducing experimentally measured (n,γ) cross section of the stable isotopes using Hauser-Feshbach model calculations to justify the adopted γSFs. Finally, the (n,γ) cross section of the unstable isotope can be predicted.

3.3.1 Final results of the photoneutron measurements

The photoneutron measurements and the extraction of a monochromatic approximation of the (γ,n) cross section have been discussed in detail in Chap. 2. Until this point we have assumed that the beam is monochromatic, while it in fact has a certain spread in energy (≈ 1-2%). In the last stage of the data analysis, we seek to account for this by using an iterative method to extract the non-monochromatic cross sections. We correct for the energy spread of the γ-ray beam, using a Taylor expansion method adapted to solve the integral of Eq. (2.4) with respect to $\sigma(E)$ [123]:

$$\sigma(E_{\mathrm{av}}) + \sum_i s_i(E_{\mathrm{av}}) = \frac{n_n}{N_t N_\gamma \xi \varepsilon_n}, \tag{3.38}$$

where

$$s_i(E_{\mathrm{av}}) = \frac{1}{n!}\sigma^{(i)}(E_{\mathrm{av}}) \int_{S_n} n_\gamma (E_\gamma - E_{\mathrm{av}})^i. \tag{3.39}$$

where $\sigma^{(i)}(E_{\mathrm{av}})$ represents the i'th derivative of $\sigma(E_{\mathrm{av}})$. To find the cross section as a function of energy, it is necessary to assume an energy dependence of the cross sections in order to calculate the s_i terms. Therefore, an iteration procedure must be applied. The iteration procedure consists of the following four steps:

1. As the first trial function, we use the monochromatic cross section $\sigma_{(0)}(E_{\mathrm{av}}) = \sigma_{\mathrm{mono}}(E_{\mathrm{av}})$. We fit this function with a Lorentzian function,

$$\sigma(E) = \sigma_c \left(\frac{E - S_n}{S_n}\right)^p \frac{1}{1 + (E^2 - E_R^2)^2/(E^2\Gamma^2)}, \tag{3.40}$$

   where σ_c, p, E_R and Γ are treated as free parameters, as done in Ref. [111].

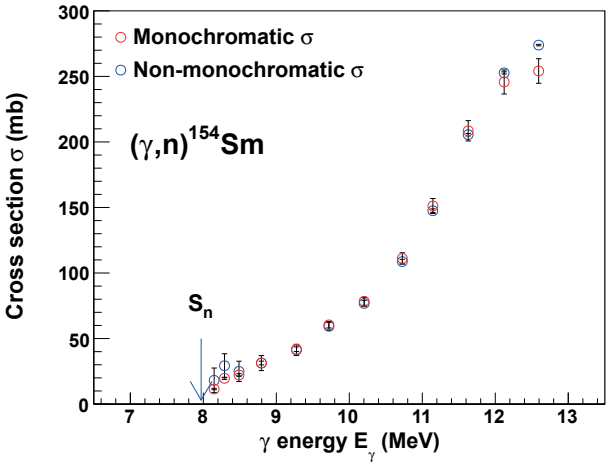

Figure 3.9: *The calibrated monochromatic and non-monochromatic* (γ,n) *cross section of* ^{154}Sm.

2. The fitted function $\sigma(E)$ is further divided into small regions of 300 keV, each region is fitted by a third order polynomial.

3. The third order polynomials are in turn used to calculate the derivatives $\sigma^{(i)}(E_{\rm av})$, of Eq. (3.39).

4. Combining the expression for the monochromatic cross section, $\sigma^{\rm mono}(E_{\rm av}) = \frac{N_n}{N_t N_\gamma \xi \varepsilon_{ng}}$ and Eq. (3.38), we solve for $\sigma(E_{\rm av})$,

$$\sigma_{(1)}(E_{\rm av}) = \sigma_{\rm mono}(E_{\rm av}) + S_2(E_{\rm av}) + S_3(E_{\rm av}). \tag{3.41}$$

   The calculated photoneutron cross section $\sigma_{(1)}(E_{\rm av})$ is used for the next iteration, and we continue until a convergence is reached.

By using a third order polynomial fit, the higher order terms in Eq. (3.38) vanish, because $\sigma^{(i)}(E_{\rm av}) = 0$, for $i > 3$. Also the s_1 term cancels out. We observe that the series converges rather rapidly, usually within $5-10$ iterations.

The overall correction for the energy spread of the γ beam is negligible, since the energy spread of the γ beam is indeed very narrow. Only cross sections located at the highest average energy will have a significant correction, as seen in Fig. 3.9.

3.3.2 Extrapolating the γSFs

The measured photo-neutron cross sections, σ, are related to the downward γSF, $\overleftarrow{f(E_\gamma)}$, by

$$\overleftarrow{f(E_\gamma)} = \frac{1}{3\pi^2\hbar^2c^2}\frac{\sigma(E_\gamma)}{E_\gamma}. \tag{3.42}$$

The radiative decay of a neutron capture state will proceed in a cascade of γ transitions. As a result, the downward γSF for E_γ lower than S_n governs the process, not the actual measured upward γSF (see Fig. 3.10). The principle of detailed balance [44], giving $\overleftarrow{f} \approx \overrightarrow{f}$, is used. Photoneutron cross sections provides a stringent experimental constraint in absolute scale on the γSF around S_n. Immediately above S_n, the γSF is of direct relevance to the p-process nucleosynthesis. Previously, the γSF method has been used to study e.g. both the production and destruction of the p-nucleus ^{94}Mo [124]. However, the (n,γ) cross sections that are relevant to the r- and s-process are sensitive to the distribution of the primary γ rays in the cascade starting from the initial capture state. Thus, the vital input in statistical Hauser-Feshbach type calculations of the neutron capture cross section is found in the energy region of several MeV below S_n (see Fig. 3.11). The predicted tail of the γSF at low energies therefore plays a fundamental role. Auxiliary data from (γ,γ') or/and particle-γ coincidence data, are extremely valuable in constructing the γSF below S_n, and are coupled together with the photoneutron data if avaliable. In the present investigations, no such data on Sm and Nd isotopes existed. The extrapolations of the measured γSF to the low energy region relies on theoretical descriptions, and were estimated by fitting microscopic models to the measured points. The reader is referred to Paper IV and V for details of these

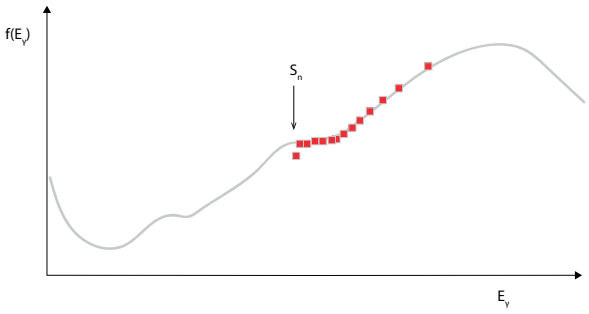

Figure 3.10: *The γSF can be inferred for γ energies ranging from the particle threshold to ∼13 MeV from the (γ,n) experiments.*

microscopic models and the fitting procedure. As a validation of our choice of an appropriate model for the γSFs, we use them as input in TALYS calculations (together with an appropriate model of the neutron-nucleus optical potential and a microscopic description of the level density) of neutron capture cross sections. The results are compared to experimentally measured (n,γ) cross section for the stable isotopes.

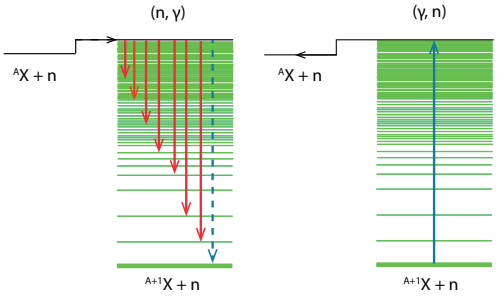

Figure 3.11: *The figure to the right represents the photoneutron reaction on a target nucleus in its ground state. The dotted line in the figure to the left represents the direct decay to the ground state, the red arrows represent the first-generation γ rays.*

3.3.3 Extracting (n,γ) cross sections

At this point in the analysis, we are prepared to extract the neutron-capture cross section of the radioactive isotope of interest based on our careful consideration of the behaviour of the neighbouring stable isotopes. See Papers IV and V for a more in-depth description of this final step of the method.

Chapter 4

Articles

The following papers are included in this thesis:

I T. Renstrøm, H.-T. Nyhus, H. Utsunomiya, S. Goriely, R. Schwengner, A. D. M. Filipescu, I. Gheorghe, L. A. Bernstein, D. L. Bleuel, T. Glodariu, A. Görgen, M. Guttormsen, T. W. Hagen, A. C. Larsen, Y.-W. Lui, D. Negi, I. E. Ruud, T. Shima, S. Siem, K. Takahisa, O. Tesileanu, T. G. Tornyi, G. M. Tveten, M. Wiedeking, *Low-energy enhancement in the γ-ray strength functions of* ^{73,74}Ge, to be submitted to Phys. Rev. C.

II A. Spyrou, S. N. Liddick, A. C. Larsen, M. Guttormsen, K. Cooper, A. C. Dombos, D. J. Morrissey, F. Naqvi, G. Perdikakis, S. J. Quinn, T. Renstrøm, J. A. Rodriguez, A. Simon, C. S. Sumithrarachchi, R. G. T. Zegers, *Novel technique for Constraining r-Process (n, γ) Reaction Rates*, Phys. Rev. Lett **113**, 232502 (2014).

III T. Renstrøm, A. Avdeenkov, O. I. Achakovskiy, B. Alex Brown, A. Bürger, A. Görgen, M. Guttormsen, S. P. Kamerdzhiev, A. C. Larsen, H .-T. Nyhus, S. Siem, G. Tveten, A. V. Voinov, *Resonances in* ^{59,60}*Ni compared with shell-model - and QTBA calculations*, to be submitted to Phys. Rev. C.

IV H.-T. Nyhus, T. Renstrøm, H. Utsunomiya, S. Goriely, D. M. Filipescu, I. Gheorghe, O. Tesileanu, T. Glodariu, T. Shima, K. Takahisa, Y.-W. Lui, S. Hilaire, S. Péru, M. Martini, and A. J. Koning, *Photoneutron cross sections for neodymium isotopes: toward a unified understanding of* (γ, n) *and* (n, γ) *reactions in the rare earth region I*, Phys. Rev. C (2015).

V D. M. Filipescu, I. Gheorghe, H. Utsunomiya, S. Goriely, T. Renstrøm, H.-T. Nyhus, O. Tesileanu, T. Glodariu, T. Shima, K. Takahisa, Y.-W. Lui,

S. Hilaire, S. Péru, and A. J. Koning, *Photoneutron cross sections for samarium isotopes: toward a unified understanding of (γ,n) and (n,γ) reactions in the rare earth region II*, Phys. Rev. C (2014).

4.1 A brief introduction to the papers

Paper I

Extensive experimental efforts were directed towards probing the γSF of ^{74}Ge through different reactions. The nucleus of choice was investigated using the following set of beams = $\{p, \alpha, ^3\text{He}, \gamma\}$. Paper I constitutes the independent contribution of the author of this thesis to the ^{74}Ge campaign. NLDs and γSFs below S_n of ^{73,74}Ge have been extracted from primary γ-ray spectra using the Oslo method. In the case of ^{74}Ge, photo-neutron cross sections have in addition been measured from right above S_n to $\sim$13 MeV, giving in total a γSF in the range between $\sim$ 1 MeV to 13 MeV. A previously reported low-energy enhancement in the γSF is reported in both germanium isotopes. Shell-model calculations of the $M1$ part of the γSF of ^{74}Ge exhibit an enhancement for low γ energies in accordance with the experimental findings. A careful analysis of the uncertainties connected with different normalization procedures are performed, and first ever experimentally constrained neutron capture cross sections of ^{72,73}Ge are deduced within these uncertainties. The influence of the low-energy enhancement on reaction rates in two different r-process environments is considered.

The author of this dissertation was responsible for planning and performing the charged particle experiment on ^{74}Ge conducted at OCL (2012), and the photoneutron experiment on ^{74}Ge at NewSUBARU (2013). The analysis of the resulting three datasets, was also performed by the author. The software used in the analysis of the NewSUBARU data was developed by the author (in collaboration with H. T. Nyhus).

Paper II

Motivated by the fact that the astrophysical site of the r-process is still undetermined, in spite of being responsible of producing $\approx$50% of the elements heavier than iron, intense efforts are directed towards reducing the nuclear physics input in the r-process modeling. The two statistical properties γSF and NLD of unstable isotopes constitute such input. In Paper II, a new method, called the β-Oslo method, demonstrates the viability of measuring the γSF and NLD of unstable nuclei using the traditional Oslo method. Excited states of ^{76}Ge were populated in β-decay from ^{76}Ga and from the following γ-decay, we were able to extract NLD and γSF of ^{76}Ge which could be used as input in Hauser-Feshbach based calculations. The publication serves as a proof-of-principle of the new method, and its main result is a first ever experimentally constrained neutron-capture cross section of the unstable isotope ^{75}Ge. The low-energy enhancement found in ^{73,74}Ge is shown to persist in this slightly more neutron-rich ^{76}Ge.

The author of this thesis contributed with NLD and γSF data from ^{74}Ge and contributed to the writing of the paper.

Paper III

Large-scale shell-model calculations of the $M1$ part of the γSFs of ^{59,60}Ni have been performed, and show a clear enhancement in the low-energy part. These new calculations are presented in Paper III, together with experimental data on the total γSF extracted from particle-γ measurements performed at OCL. New QTBA calculations on the $E1$ part of the γSF have been performed and together with the $M1$ calculations, they excellently reproduce the experimental measured data.

The author of this thesis was responsible for the planning and performance of the charged-particle experiment on ^{60}Ni conducted at OCL, performed the data analysis and wrote the paper.

Paper IV and V

With the goal of constraining the neutron capture cross section of the s-process branch point nucleus, ^{147}Nd, and the short-lived isotope ^{151}Sm, extensive measurements on photo-neutron cross sections of in total 12 stable Sm and Nd isotopes have been performed (2013). The experiments were conducted at the NewSUBARU synchrotron laboratory, using practically monoenergetic LCS γ-ray beams. The photo-neutron cross sections where extracted from the neutron separation threshold of each isotope up to $\approx$ 13 MeV. The radiative neutron-capture cross-section where deduced using the indirect γSF method. The present systematic measurements included two odd-N Nd nuclei, ^{143}Nd and ^{145}Nd for which photo-neutron cross sections are measured near neutron threshold for the first time. Photo-neutron cross sections for two odd-N Sm nuclei, ^{147}Sm and ^{149}Sm, are also measured for the first time. The present photo-neutron measurement also involved a p-process nucleus ^{144}Sm, s-only nuclei ^{148}Sm and ^{150}Sm and an r-only nucleus ^{154}Sm.

The author participated in the two experiments, developed the analysis software and analysed all 12 sets of (γ,n) data (in collaboration with H.T. Nyhus), wrote the Paper IV in collaboration with H.T. Nyhus, and contributed to the writing of Paper V.

Chapter 5

Discussion of results, conclusions and outlook

The inaccessibility of the neutron capture cross sections for certain unstable nuclei which could have a significant impact on nucleosynthetic processes has motivated this thesis. Indirect determination of the (n,γ) cross section can be reached in statistical Hauser-Feshbach calculations. The main problem to date has been the lack of actual experimentally measured input function into this formula. In this work such input in the form of NLDs and γSFs have been extracted. Great emphasis has been put on revealing structures in the γSF below S_n, such as the low-energy enhancement. The most interesting findings will in the following be summarized and further discussed in light of recent and highly exciting new data and shell-model calculations.

5.1 Summary of results

In the experiments that constitute this thesis a wide variety of reactions have been induced in different nuclei in order to reveal some of their statistical properties. NLDs and γSFs in ^{59,60}Ni and ^{73,74,76}Ge have been extracted through a statistical analysis of first-generation γ spectra, and photo-neutron cross sections of $^{143-146,148}$Nd and $^{144,147-150,152,154}$Sm nuclei have been deduced through photo-absorption experiments. Interestingly, we found that for all Ni and Ge isotopes explored, the previously reported low-energy enhancement was observed in their respective γSFs. These enhancements were reproduced in shell-model calculations of the $M1$ component of the γSFs in ^{59,60}Ni and ^{74}Ge.

Furthermore, the data obtained from investigations of Ni, Ge, Nd and Sm isotopes were used as input in statistical Hauser-Feshbach calculations, for the first time giving the following five data-constrained (n, γ) cross sections :

- ^{72,73}Ge(n,γ)
- ^{75}Ge(n,γ)
- ^{147}Nd(n,γ)
- ^{153}Sm(n,γ)

where ^{72,73}Ge are stable, whereas ^{75}Ge, ^{147}Nd and ^{153}Sm are unstable with half-lives of 82.8 s, 10.98 d and 1.9 d, respectively. Two indirect techniques were applied in the deduction of the neutron-capture cross sections: for the rare earth isotopes, the γSF method was used, whereas for extraction of the ^{75}Ge(n,γ) cross section, the recently developed β-Oslo method was employed.

Finally, we calculated stellar reaction rates for neutron-rich Ge isotopes which showed a potentially large effect of a low-energy enhancement in the the weak r-process, if it persists in exotic nuclei.

5.2 Reaction-independent γSFs

A prominent part of the motivation behind the joint ^{74}Ge experimental effort was to answer the question of whether γSFs are reaction-dependent. To this end, a specific nucleus was studied using a wide range of probes and different experimental methods.

In Fig. 5.1, the γSFs of ^{74}Ge extracted from three different nuclear reactions are presented. Below S_n, the results of inelastic scattering of γ rays, (γ,γ') and the charged-particle induced reaction, (^{3}He,^{3}He$'\gamma$), are plotted. These two reactions are fundamentally different ways of probing the γSF, as the former is a photoexcitation reaction, populating mainly 1- states, while the latter measures the photodeexcitation from states within a broad spin range, $\approx$ 0-10$\hbar$, in the quasicontinuum of ^{74}Ge. Still, a surprisingly good agreement is seen in the γSFs from these two reactions. Furthermore, there seems to be a rather seamless transition between the two datasets below S_n and the newly measured photoneutron data just above S_n. However, some inconsistencies in the shape of the γSF of ^{74}Ge have been reported. In Fig. 5.1 an enhancement centered at $\sim$ 7 MeV is seen in the data from the (^{3}He, ^{3}He$'\gamma$) experiment. This structure is also found in the data from the (α,$\alpha'\gamma$) reaction investigated at iThemba LABS, and interpreted as being a pygmy resonance [125]. This reported enhancement in the $E1$ strength is not obvious in the photonscattering reaction, but the error bars are very large in this energy region and it is hard to draw any firm conclusions. Moreover, the low-energy enhancement was unfortunately inaccessible in the photonscattering reaction, while in the (α,$\alpha'\gamma$) data it was unresolved. Preliminary results from the ($p, p'\gamma$) reaction however, show clear signs of a low-energy enhancement [125].

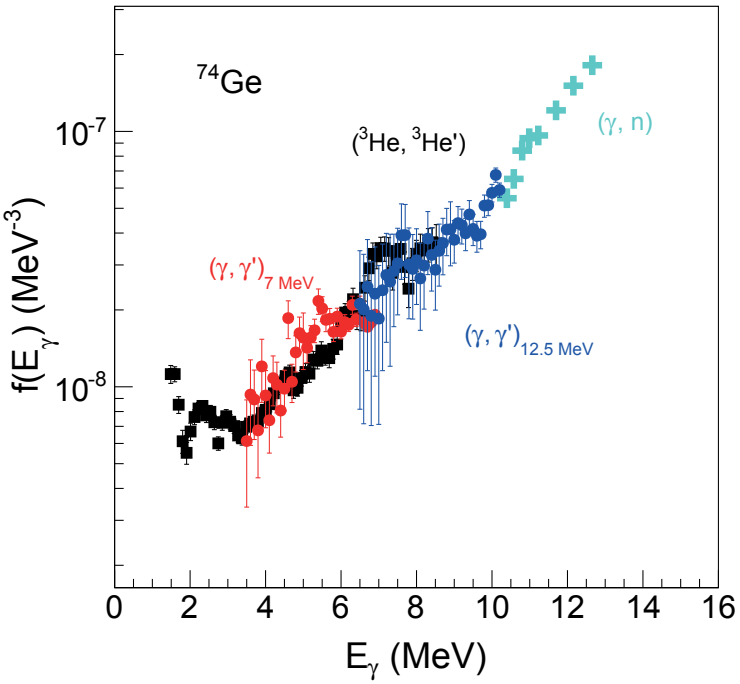

Figure 5.1: *γSF of ^{74}Ge obtained from photonscattering reactions utilizing electron beams of 7 MeV and 12.5 MeV (red and blue circles, respectively) [126], from a statistical analysis of primary γ-ray spectra (black squares) and from (γ, n) reactions (green crosses).*

With the motivation of constraining the neutron capture cross section of ^{75}Ge, the γSF of ^{76}Ge was measured using the β-Oslo method. The Gamow-Teller β decay of ^{76}Ga to the daughter nucleus, ^{76}Ge, mainly populates states with spins $J = 1, 2$ and 3 and positive parity since the ground state of ^{76}Ga has spin/parity 2^+ [127]. In spite of the difference in populated spin range, there is a surprisingly good agreement between ^{76}Ge and the ^{74}Ge γSF data obtained with the standard Oslo method. The two data sets also show a low-energy enhancement of similar strength. This indicates a spin independence of the low-energy enhancement. This point has previously been discussed in connection with the significantly deviating

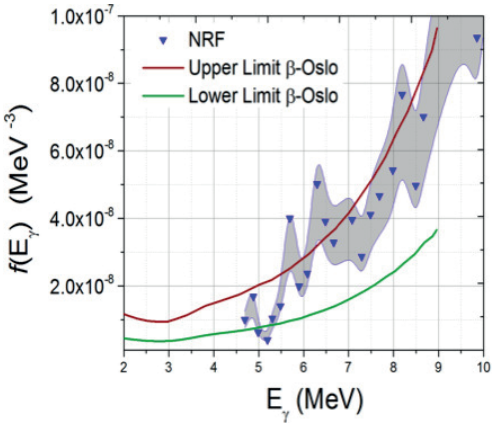

Figure 5.2: *The γSF of ^{76}Ge obtained through NRF measurements (blue triangles, uncertainty band given in grey), and through a statistical decay of the primary- γ rays from ^{76}Ge populated in β-decay from ^{76}Ga (red and green line) [100]. The figure is taken from Ref. [128]*

results on the γSFs in the case of molybdenum (see Fig. 1.5). Furthermore, a photonscattering experiment on ^{76}Ge, populating states of spin $J = 1^-, 1^+, 2^+$, gives results close to the upper limit of the β-Oslo experiment, as observed in Fig. 5.2 (from Ref. [128]).

In conclusion, the multiple Ge experiments seem to suggest that the resulting γSFs are not necessarily very sensitive to the parity or spin of the initially populated states in the various reactions used.

5.3 The low-energy enhancement

As reported in Paper I,II and III, a low-energy enhancement is found in the γSFs of ^{59,60}Ni and ^{73,74,76}Ge. See Fig. 5.3. Similar enhancements in the very low γ-energy region were found in shell-model calculations of the $M1$ strength in ^{59,60}Ni and ^{74}Ge, as shown in Fig. 5.4.

The results of the shell-model calculations support the theoretical works of Refs. [47, 48], where the low-energy enhancement is argued to be of $M1$ type. Still, it does not exclude contributions from $E1$ radiation (as suggested in Ref. [82]). Shell-model calculations of the $E1$ strength require an inclusion of the next main shell to account for the parity change in the transitions, involving an expansion

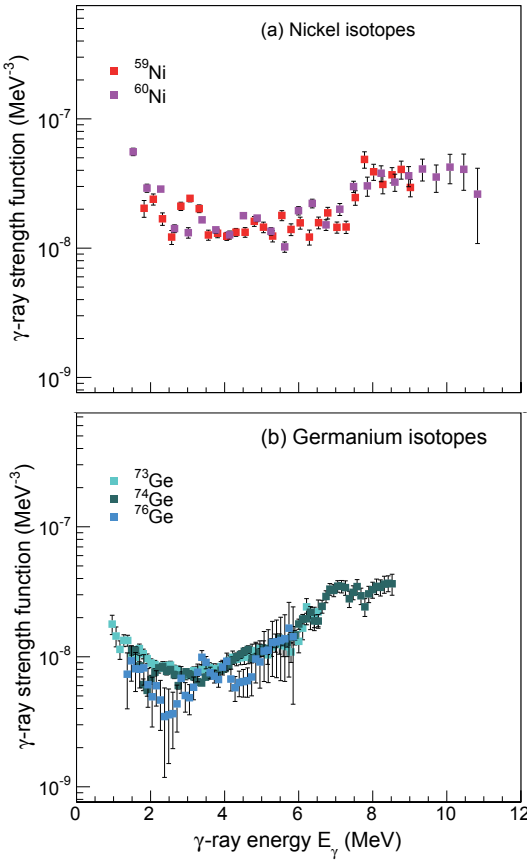

Figure 5.3: *Low-energy enhancements discovered in (a) Ni and (b) Ge isotopes (Paper I and II).*

of the configuration space. This is a very challenging task, but is presently under consideration [129]. Assuming that the low-energy enhancement is mainly due to $M1$ transitions in the quasicontinuum, there exist two different physical interpretations of this phenomenon. According to the authors of Ref. [47], the extra strength is analogous to the shears mechanism, and appears between states with equal configurations by recoupling of certain proton *and* neutron spins in high-j orbits and with large magnetic moments. As a consequence, there will be

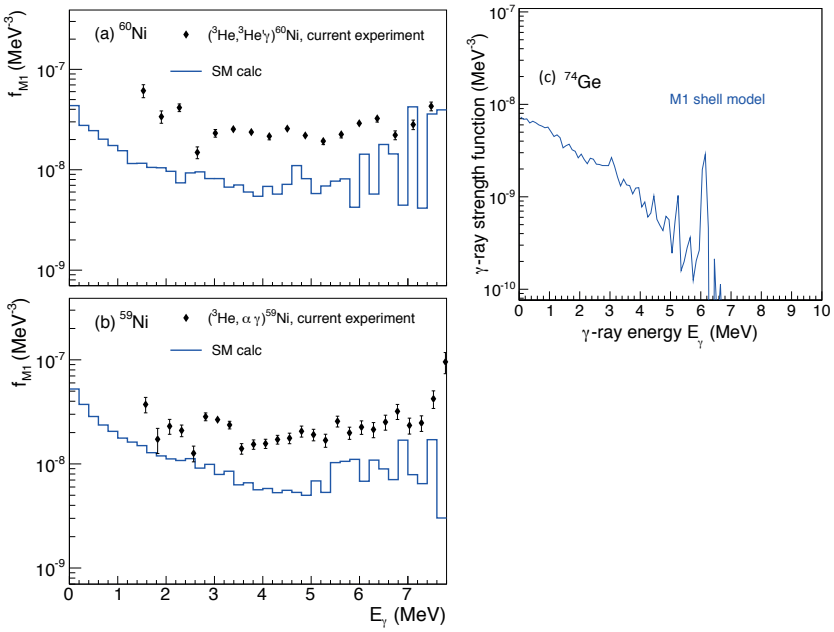

Figure 5.4: *Shell-model calculations of the $M1$ strength in ^{59,60}Ni (blue histogram) and ^{74}Ge (blue line). In the case of ^{59,60}Ni (black squares) the calculations are compared with data from OCL. The figures are taken from Paper I and II.*

certain regions in the nuclear chart where isotopes are expected to have a low-energy enhancement in their $M1$ strength. This view is not shared by the authors of Ref. [48], who advocate that $0\hbar\omega$ transitions are responsible for the enhancement in the low-lying strength. These types of transitions should be present in all nuclei, so a low-energy enhancement would be expected throughout the nuclear chart. Recent experimental data supports this last theory of an ubiquitous low-energy enhancement; for the first time this structure is found in the γSF of well deformed rare earth isotopes, ^{151,153}Sm [114]. The Sm measurements were performed at Texas A&M, using Compton-supressed Ge clover detectors, allowing an extraction of the γSF in a γ-energy range previously inaccessible for rare earth isotopes in traditional Oslo experiments. As seen in Fig. 5.5, the Sm isotopes are rather far away from the regions where we expect to find magnetic rotation (see

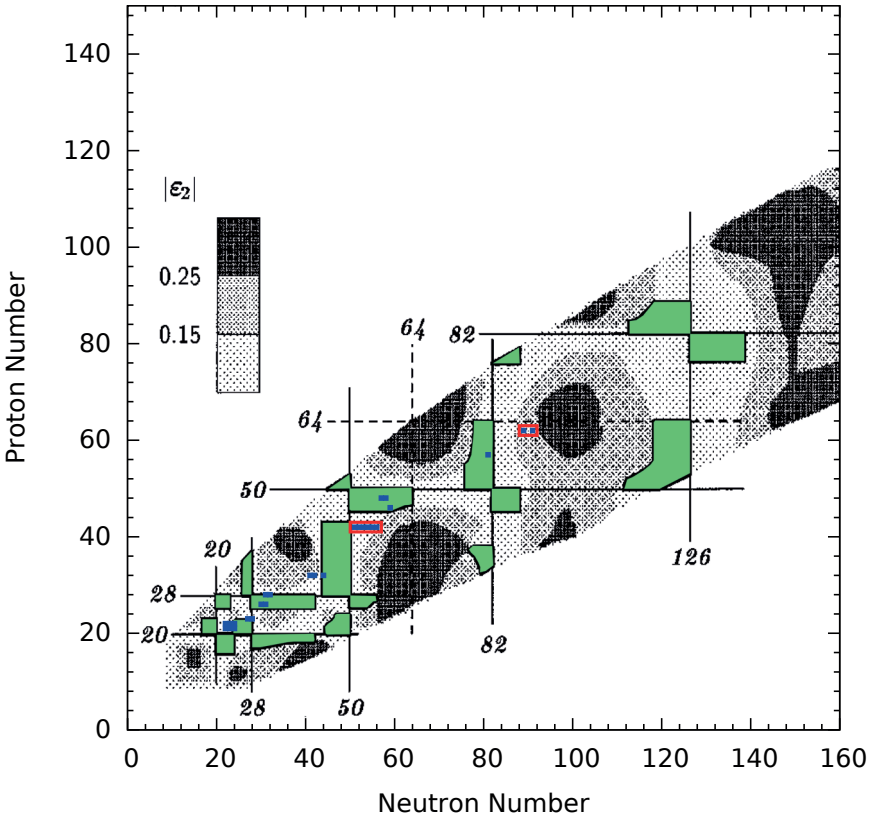

Figure 5.5: *The appearance of magnetic rotation in different mass regions enclosed by thick lines and green filling. The figure is adapted from [130]. All reported nuclei exhibiting a low-energy enhancement in the γSF investigated by the Oslo method are indicated by blue squares and are marked by red rectangles when far from the areas of magnetic rotation.*

red rectangle to the right). In addition, we notice that the more neutron-rich Mo isotopes are quite far away from the green areas. These findings support the view that this low-energy enhancement is not connected to specific regions, but could indeed appear throughout the nuclear chart.

The effect of the low-energy enhancement on the reaction rates involving

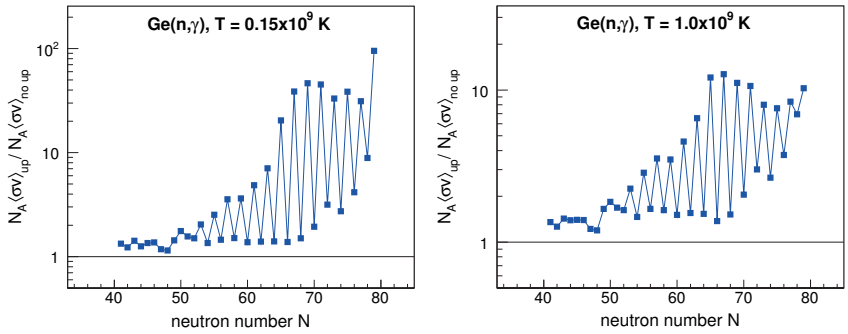

Figure 5.6: *Ratios of neutron capture reaction rates (blue squares) including low-energy enhancement relative to rates excluding the low-energy enhancement [131].*

neutron-rich nuclei in the r-process has been investigated and presented in several publications, e.g. Ref. [79]. This is often illustrated effectively in the form of a ratio between the rate of neutron capture including the low-energy enhancement, and the rate omitting the low-energy enhancement. We have also calculated this rate for two different temperatures of the unknown r-process environment. As shown in Fig. 5.8, the impact of the low-energy enhancement on the rates is considerable.

Until recently, no existing theoretical calculations on the γSF could predict the apperence the low-energy enhancement. However, armed with shell-model calculations, we find ourselves in a new situation, where we are able to predict the existence of the low-energy enhancement. The first shell-model calculation of the low energy $M1$ component of the γSF of the neutron-rich ^{80}Ge has recently been performed [126], and exhibits a clear enhancement at low γ energies, see Fig. 5.7. Because several stable isotopes of Ge are now thoroughly investigated through multiple experiments, a progression towards more neutron-rich isotopes becomes very intriguing. The main goal is to reach ^{81}Ge, which is predicted to be very important for the weak r-process [25].

During the winter of 2015, the first dedicated β-Oslo experiment was performed at NSCL/MSU. One isotope of particular interest from that experiment is ^{70}Ni, by far the most neutron-rich isotope investigated using the Oslo method (in terms of the N/Z-ratio). A clear low-energy enhancement is shown in ^{70}Ni, as displayed in Fig. 5.8. In this work, the low-energy enhancement has been shown to exist in ^{59,60}Ni, and now it has been found to persist with the addition of ten

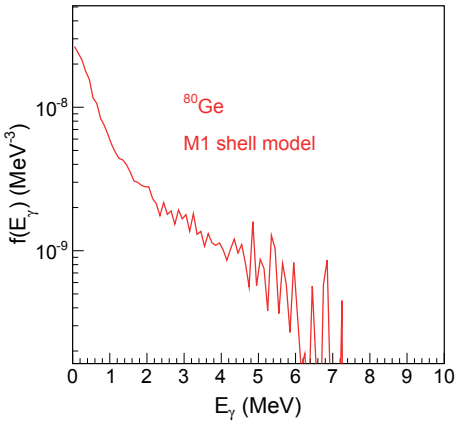

Figure 5.7: *Shell-model calculations of the M1 strength in the neutron-rich germanium isotope ^{80}Ge. The figure is taken from Ref. [126].*

more neutrons.

In conclusion, both the theoretical predictions regarding ^{80}Ge and the experimental results on ^{70}Ni indicate that the low-energy enhancement will persist in more exotic, neutron-rich nuclei and therefore possibly effect r-process calculations. This renders further experimental investigations necessary to prove or disprove whether this resonance-like structure truly is present throughout the nuclear chart.

5.4 Outlook

Investigating the character and multipolarity of the low-energy enhancement is an experimental challenge. Several plans are devised to study this feature, see for example Ref. [132]. As for the persistence of this low-energy enhancement, moving towards more neutron-rich isotopes, the β-Oslo method is a promising technique as long as $Q_\beta \approx S_n$ and the β-n branch is not very large. Therefore, we would like to use this method for investigations of more neutron-rich Ge isotopes, and an experiment at NSCL/MSU has been proposed. The present radioactive ion beam facility at NSCL will be upgraded to Facility of Radioactive Ion Beam (FRIB), providing a higher intensity of short-lived exotic nuclei. This facility will provide access to nuclei that are currently only reached at RIKEN.

An experiment using a ^{66}Ni beam of 5.5 MeV/u has been granted beam time at HIE-ISOLDE [133]. The motivation behind this experiment is to use the Oslo method on data from an inverse kinematics radioactive-beam experiment, and continue the systematic work of mapping the properties of Ni isotopes as a function of neutron number. The data will also be analysed using the TSC method. Already a test-experiment using inverse kinematics via the ^{86}Kr(d,p)^{87}Kr has been successfully performed at iThemba LABS and the data are under analysis.

A new systematic study using the γSF method is under preparation. The idea is to combine results provided by OCL on γSFs below S_n, extracted from ^{205}Tl$(p,p'\gamma)$, ^{205}Tl$(p,d\gamma)$ and ^{205}Tl$(d,p\gamma)$ reactions, with results from NewSUBARU on γSFs above S_n, extracted from (γ,n) measurements on ^{205}Tl and ^{203}Tl. The goal is to determine the ^{204}Tl neutron capture cross section. Some photoneutron data exists on ^{203}Tl, but no information is available on ^{205}Tl. However, ^{205}Tl plays an important role in nuclear astrophysics, as it is directly linked to the extinct radionuclide ^{205}Pb of potential cosmochemical interest. For a detailed theoretical study of the nuclear physics and astrophysics aspects of the ^{205}Tl-^{205}Pb pair see Refs. [134, 135]. The measurement of the ^{205}Tl photoneutron cross section will directly constrain the neutron-capture cross section of ^{204}Tl, in combination with

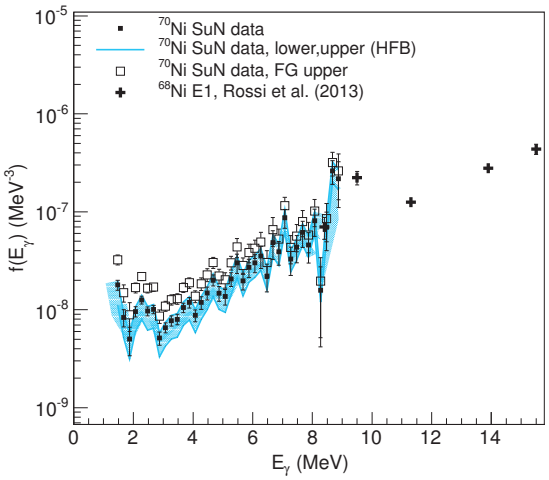

Figure 5.8: *The γSF of ^{70}Ni deduced from data obtained in a β-Oslo experiment. Included in the plot are data from Ref. [91]. The figure is taken from Ref. [90].*

the measurements from OCL, through the γSF method. Consequently, this will impact the s-process production of ^{205}Tl and ^{205}Pb. If there is a significant ^{205}Pb production by the s-process, it could allow the development of a new s-process chronometry based on the ^{205}Tl-^{205}Pb pair.

5.5 Future upgrades

The nuclear physics group in Oslo has recently acquired two $3.5'' \times 8''$ $LaBr_3$ detectors. They are superior to the existing array of NaI detectors (CACTUS) with respect to efficiency and resolution, see Fig. 5.9. The two detectors were taken into use for the first time in the Kr experiment at iThemba LABS, April-May 2015. Our future goal is to exchange our NaI array with 30 $LaBr_3$ detectors. An infrastructure grant application of 21 million NOK to the Research Council of Norway has recently been accepted, and the project of replacing CACTUS with Oslo Scintillator Array (OSCAR) of $3.5'' \times 8''$ cylindrical $LaBr_3$:Ce detectors will start in the near future.

A new facility, Extreme Light Infrastructure-Nuclear Physics (ELI-NP), located at Magurele-Bucharest, Romania, will in the future provide very powerful, nearly monochromatic γ-ray beams. The produced beams will cover a large energy range: $E_\gamma = 0.2$ -19 MeV, and have extreme intensities: $I_\gamma \geq 10^{11}$ (s^{-1} mm^{-2} $mrad^{-2}$ 0.1-1%), and resolutions $\Delta E/E \leq 0.5\%$ will be obtained. At this facility, measurements similar to the New-SUBARU experiments can be performed. Due to the high granularity of the proposed γ and neutron detector arrays, one expects to be able to measure the multipolarity of the emitted γ rays (below the neutron separation energy) and neutrons (above the neutron separation energy), and the multipole mixing by measuring the angular distributions. Given the fact that the incident γ beam will be almost 100% polarized, it should be possible to determine the electromagnetic character of the emitted γ rays (and similar for neutrons) by looking at the correlation of direction of emitted particles with the polarization plane. Similar measurement are currently performed at HIγS [136]. ELI-NP was approved by the European Commission in September 2012, and the first experiments are planned to take place in 2018.

In summary, there is at present high activity and major efforts to develop methods and detectors in the field of nuclear physics, and upcoming new facilities are under construction. Therefore, the prospects of understanding nuclear properties in the quasicontinuum as a function of mass and isospin are very promising. Intense theoretical and experimental efforts have been made towards shedding light on the γSF and in particular the low-energy enhancement. An experimental determination of the electromagnetic character, and on the theoretical side the physical mechanism of this structure, is a goal for the future. The unveiling of the

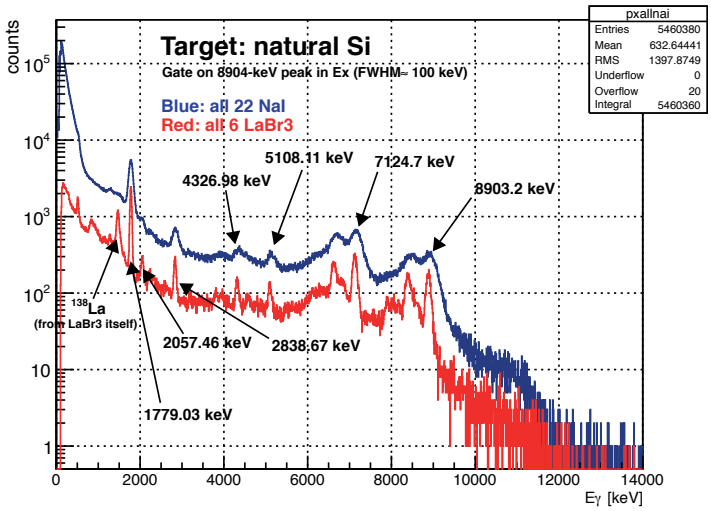

Figure 5.9: *The γ-ray spectrum of natural Si with a gate on the 8.9-MeV level in ^{28}Si, excited in the $(p,p'\gamma)$ reaction with E_p = 16 MeV, measured with an array of 22 5"×5" NaI(Tl) detectors and 6 3.5"×8" LaBr$_3$(Ce) detectors from the Milano HECTOR$^+$ array. The spectrum was measured in connection with the Fe experimental campaign [81].*

mechanisms behind the low-energy enhancement will have a large impact on the understanding of the γSF of nuclei, and this knowledge will possibly have a great impact on astrophysical network calculations.

Appendix A

New intensities and FWHMs deduced for the NaI response functions

Ref. [112] describes the unfolding procedure used in the Oslo method. However, new and improved measurements of the response functions of the NaI detectors have recently been performed. New intensities and FWHMs deduced for the NaI response functions are given in Table A.1. The response functions are measured for several in-beam γ lines from excited states in ^{13}C, ^{16,17}O, ^{28}Si and ^{56,57}Fe [113]. To obtain best possible results of the unfolding, the resolution of the response functions are currently set to 10% of the experimental resolution, and not 50% as cited in Ref. [112].

E_γ (keV)	FWHM[keV][a]	$\varepsilon^b_{\text{tot}}$	p_f	p_c	p_s	p_d	p_a
800.0	72.8	0.923	0.5778	0.4222	0.0000	0.0000	0.0000
1600.0	103.1	1.003	0.3968	0.5896	0.0097	0.0000	0.0039
2400.0	135.7	1.023	0.3135	0.6537	0.0180	0.0000	0.0148
3200.0	163.9	1.037	0.2443	0.6918	0.0340	0.0071	0.0227
4000.0	188.2	1.045	0.1970	0.7059	0.0444	0.0086	0.0441
4800.0	207.3	1.053	0.1599	0.7256	0.0525	0.0092	0.0529
5600.0	222.7	1.059	0.1435	0.7489	0.0577	0.0084	0.0415
6400.0	238.6	1.066	0.1296	0.7671	0.0590	0.0081	0.0362
7200.0	263.5	1.071	0.1200	0.7760	0.0524	0.0089	0.0427
8000.0	287.4	1.073	0.1102	0.7850	0.0458	0.0096	0.0493
8800.0	310.2	1.076	0.0999	0.7953	0.0389	0.0104	0.0556
9600.0	331.9	1.079	0.0897	0.8054	0.0321	0.0111	0.0619
10400.0	351.9	1.081	0.0830	0.8126	0.0307	0.0113	0.0623

[a] Normalized to 79.9 keV (6%) at 1.33 MeV.
[b] Normalized to 1 at 1.33 MeV.

Table A.1: The new intensities and FWHMs deduced for the NaI response functions.

List of Figures

List of Tables

Bibliography

[1] H. Kragh, *Quantum Generations: A History of Physics in the Twentieth Century*, Princeton University Press (2002).

[2] E. Rutherford, Proc. Roy. Soc. A **90**, (1914).

[3] A. Pais, *Inward Bound: Of matter and forces in the physical world*, Oxford University Press (1988), p. 398.

[4] G. Gamow, Clarendon Press, Oxford, p.5 (1931).

[5] J. Chadwick, Proc. Roy. Soc., A, **136**, 692 (1932).

[6] H. Kragh, *Cosmology and Controversy: The historical Development of Two Theories of the Universe*, Princeton, NJ: Princeton University Press (1996).

[7] H. A. Bethe, Phys. Rev. **55**, 434 (1939).

[8] H. Kragh, *Quantum Generations, A history of physics in the twentieth century.* Princeton university press (1999).

[9] V. M. Goldschmidt, J. Chem. Soc., 655 (1937).

[10] O. Pedersen og H. Kragh, *Fra kaos til kosmos, Verdensbildets historie gjennom 300 år*. Samlernes bogklub, p.304 (2003).

[11] F. Hoyle, Astrophysical Journal Supplement, vol. **1**, 121 (1954)

[12] D. N. F. Dunbar *et al.*, Phys. Rev. **92**, 649 (153).

[13] H. E. Suess and H. C. Urey, Rev. Mod. Phys. **28**, 53 (1956).

[14] M. Goeppert-Mayer, Phys. Rev. **75**, 1969 (1949).

[15] O. Haxel, J. H. D. Jensen, and H. E. Suess, Phys. Rev. **75**, 1766 (1949).

[16] P. W. Merrill, Astrophys. J., **116**, 21 (1952).

[17] E. M. Burbidge, G. R. Burbidge, W. A. Fowler, and F. Hoyle, Rev. Mod. Phys. **29**, 547 (1957).

[18] A. G. W. Cameron, Pub. Astron. Soc. Pac. **69**, 201 (1957).

[19] A. T. Yue *et al.*, Phys. Rev. Lett. **111**, 222501 (2013).

[20] C. Iliadis, "*Nuclear Physics of Stars*", Wiley-VCH Verlag, Weinheim (2007).

[21] F. Käppeler, R. Gallino, S. Bisterzo, and W. Aoki, Rev. Mod. Phys. **83**, 157 (2011).

[22] M. Arnould, S. Goriely, and K. Takahashi, Phys. Rep. **450**, 97 (2007).

[23] R. Surman, Astrophys. J. **679**, 117 (2008).

[24] S. Wanajo, Astrophys. J. **746**, 180 (2012).

[25] R. Surman *et al.*, AIP Advances **4**, 041008 (2014).

[26] M. Arnould and S. Goriely, Phys. Rep. **384**, 1 (2003).

[27] T. Rauscher, Rep. Prog. Phys. **76**, 066201 (2013).

[28] A. Spyrou *et al.*, Phys. Rev. C **77**, 065801 (2008).

[29] M. Arnold and S. Goriely, Phys. Rep. **384**, 1 (2003).

[30] W. Hauser, H. Feshbach, Phys. Rev. **87**, 366 (1952).

[31] H. Utsunomiya *et al.*, Phys. Rev. C **82**, 064610 (2010).

[32] H. A. Bethe, Phys. Rev. **50**, 332 (1936).

[33] T. von Egidy, D. Bucurescu, Phys. Rev. C **72**, 044311 (2005), and Phys. Rev. C **73**, 049901(E) (2006).

[34] T. von Egidy and D. Bucurescu. Phys. Rev. C **80**, 054310 (2009).

[35] T. Ericson, Nucl. Phys. A **11**, 481 (1959).

[36] S. Goriely, S. Hilaire, and A.J. Koning, Phys. Rev. C **78**, 064307 (2008).

[37] S. Hilarie *et al.*, Nucl. Phys. C **86**, 064317 (2012).

[38] H. Nakada and Y. Alhassid, Phys. Rev. Lett. **79**, 2939 (1997).

[39] M. Bonett-Matiz, A. Mukherjee, and Y. Alhassid, Phys. Rev. C **88**, 011302(R) (2013).

[40] C. Özen, Y. Alhassid, and H. Nakada, Phys. Rev. C **91**, 034329 (2015).

[41] A. Voinov *et al.*, Phys. Rev C **77**, 034613 (2008).

[42] Y. Kalmykov *et al.*, Phys. Rev. Lett. **99**, 202502 (2007).

[43] A. C. Larsen *et al.*, Phys. Rev. C **83**, 034315 (2011).

[44] R. Capote *et al.*, Reference Input Library, RIPL-2 and RIPL-3, available online at
`http://www-nds.iaea.org/RIPL-3/`.

[45] G. A. Batholomew, E. D. Earle, A. J. Fergusson, J. W. Knowles. M. A. Lone, Adv. Nucl. Phys. **7** , 229 (1972).

[46] R. Schwengner, Phys. Rev. C **90**, 064321 (2014).

[47] R. Schwengner, S. Frauendorf, and A. C. Larsen, Phys. Rev. Lett. **111**, 232504 (2013).

[48] B. Alex Brown and A. C. Larsen, Phys. Rev. Lett. **113**, 252502 (2014).

[49] S. Goriely and E. Khan, Nucl. Phys. A **706**, 217 (2002).

[50] A. Avdeenkov *et al.*,Phys. Rev. C **83**, 064316 (2011).

[51] O. Achakovskiy *et al.*, Phys. Rev. C **91**, 034620 (2015).

[52] R. Schwengner *et al.*, Phys. Rev. C **87**, 024306 (2013).

[53] S. A. Sheets *et al.*, Phys. Rev. C **79**, 024301 (2009).

[54] A. M. Hoogenboom, Nucl. Instrum Methods **3**, 57 (1958).

[55] I. Poltoratska *et al.*, Phys. Rev. C **89**, 054322 (2014).

[56] J. M. Blatt and V. F. Weisskopf, *Theoretical Nuclear Physics*, Wiley, New York, (1952).

[57] M. N. Harakeh and A. van der Woude, *Giant Resonances*, Oxford Science Publications (2001).

[58] N. Lo Iudice and F. Palumbo, Phys. Rev. Lett. **41**, 1532 (1978).

[59] K. Heyde, P. von Neumann-Cosel, and A. Richter, Rev. Mod. Phys. **82**, 2365 (2010).

[60] M. Guttormsen *et al.*, Phys. Rev. Lett. **109**, 162503 (2012).

[61] M. Krtička *et al.*, Phys. Rev. Lett. **92**, 172501 (2004).

[62] A. C. Larsen *et al.*, Acta Physica Polonica B **46** (2015).

[63] P. Adrich *et al.*, Phys. Rev. Lett. **95**, 132501 (2005).

[64] U. Agvaaluvsan *et al.*, Phys. Rev. Lett. **102**, 162504 (2009).

[65] D. Savran, T. Aumann, and A. Zilges, Prog. Part. Nucl. Phys. **70**, 210 (2013).

[66] O. Wieland, Phys. Rev. Lett. **102**, 092502 (2009).

[67] I. Daoutidis and S. Goriely, Phys. Rev. C **86**, 034328 (2012).

[68] S. Goriely, Phys. Lett B **436**, 10 (1998).

[69] A. Voinov *et al.*, Phys. Rev. Lett. **93**, 142504 (2004).

[70] M. Guttormsen *et al.*, Phys. Rev C **71**, 044307 (2005).

[71] M. Krtička *et al.*, Phys. Rev. C **77**, 054319 (2008).

[72] M. Krtička and F. Bečvár, EPJ Web of Conferences **2**, 03002 (2010).

[73] A. C. Larsen *et al.*, Phys. Rev. C **73**, 064301 (2006).

[74] A. C. Larsen *et al.*, Phys. Rev. C **76**, 044303 (2007).

[75] A. C. Larsen *et al.*, Phys. Rev. C **85**, 014320 (2012).

[76] N. U. H. Syed, *et al.*, Phys. Rev. C **80**, 044309 (2009).

[77] M. Guttormsen *et al.*, Phys. Rev. C **83**, 014312 (2011).

[78] A. Voinov *et al.*, Phys. Rev. C **81**, 024319 (2010).

[79] A. C. Larsen and S. Goriely, Phys. Review C **82**, 014318 (2010).

[80] M. Wiedeking *et al.*, Phys. Rev. Lett. **108**, 162503 (2012).

[81] A. C. Larsen *et al.*, Phys. Rev. Lett. **111**, 242504 (2013).

[82] E. Litvinova and N. Belov, Phys. Rev. C **88**, 031302(R) (2013).

[83] B. V. Kheswa *et al.*, Physics Letters B **744**, 268 (2015).

[84] All published results from the Oslo group can be found at:
`http://www.mn.uio.no/fysikk/english/research/about/infrastructure/OCL/nuclear-physics-research/compilation/`

[85] The homepage of ELBE,
`https://www.hzdr.de/db/Cms?pNid=145`.

[86] The homepage of Berkeley labs,
`https://www.lbl.gov`.

[87] The homepage of iThemba labs,
`http://tlabs.ac.za`.

[88] The homepage of OCL,
`http://www.mn.uio.no/fysikk/english/research/about/infrastructure/OCL`.

[89] Homepage of NewSUBARU,
`http://www.spring8.or.jp/en/about_us/whats_sp8/facilities/accelerators/new_subaru`

[90] A. C. Larsen, Private communication, Spring 2015.

[91] D. M. Rossi *et al.*, Phys. Rev. Lett. **111**, 242503 (2013).

[92] M. Guttormsen, A. Atac, G. Løvhøiden, S. Messelt, T. Ramsøy, J. Rekstad, T. F. Thorsteinsen, T. S. Tveter, and Z. Zelazny, Phys. Scr. T **32**, 54 (1990).

[93] M. Guttormsen, A. Bürger, T. E. Hansen, and N. Lietaer, Nucl. Instrum. Methods Phys. Res. A **648**, 168 (2011).

[94] W. R. Leo, *Techniques for nuclear and particle physics experiments*, Springer Verlag, p. 24 (1994).

[95] D. J. Morrissey, B.M. Sherrill, M. Steiner, A. Stolz, and I. Wiedenhoever, Nucl. Instrum. Methods Phys. Res., Sect. B **204**, 90 (2003).

[96] A. Spyrou, presentation given at the 2015 Oslo workshop.

[97] K. Cooper *et al.*, Nucl. Instrum. Methods Phys. Res. A **763**, 543-546 (2014).

[98] A. Simon *et al.*, Nucl. Instrum. Methods Phys. Res. A **703**, 16-21 (2013).

[99] C. J. Prokop *et al.*, Nucl. Instrum. Methods Phys. Res. A **741**, 163 (2014).

[100] A. Spyrou *et al.*, Phys. Rev. Lett. **113**, 232502 (2014).

[101] S. Amano, K. Horokawa, K. Ishihara, S. Miyamoto, T. Hayakawa, T. Shizuma, T. Mochizuki, Nucl. Inst. and Meth. A **602**, 337-341 (2009).

[102] H. Utsunomiya, T. Shima, K. Takahisa, D. M. Filipescu, O. Tesileanu, I. Gheorghe, H.-T. Nyhus, T. Renstrøm, Y.-W. Lui, Y. Kitagawa, S. Amano, S. Miyamoto, IEEE Transactions on Nuclear Science **61**, (2014).

[103] The homepage of RIKEN research, `http://xfel.riken.jp/eng/gallery/index.html\#image/001-1.jpg`.

[104] J. Allison, IEEE Transactions on Nuclear Science **53**, 270-278 (2006).

[105] S. Agostinelli, NIM A **506**, 250-303 (2003).

[106] D. Filipescu *et al.*, AIP Conference Proceedings 1645, 322 (2015).

[107] T. Kondo, H. Utsunomiya, H. Akimune, T. Yamagata, A. Okamoto, H. Harada, F. Kitatani, T. Shima, K. Horikawa, S. Miyamoto, Nucl. Inst. and Meth. A **659**, 462-466 (2011).

[108] NIST Physical Measurement Laboratory, `http://physics.nist.gov/PhysRefData/XrayMassCoef/tab3.html`.

[109] H. Toyokawa, T. Kii, H. Ohgaki, T. Shima, T. Baba, and Y. Nagai, IEEE Transactions on nuclear science, Vol. **47**, No 6, (2000).

[110] B. L. Berman and F. C. Fultz, Rev. Mod. Phys. **47**, 713-761 (1975).

[111] O. Itoh, H. Utsunomiya, H. Akimune, T. Kondo, M. Kamata, T. Yamagata, H. Toyokawa, H. Harada, F. Kitatani, S. Goko, C. Nair, and Y. W. Lui, Journal of Nuclear Science and Technology, Vol. **48**, No. 5, 834-840 (2011).

[112] M. Guttormsen, T. S. Tveter, L. Bergholt, F. Ingebretsen, J. Rekstad, Nucl. Inst. Meth. A **374**, 371 (1996).

[113] M. Guttormsen *et al.*, Phys. Rev. C **89**, 014302 (2014).

[114] A. Simon *et al.*, submitted to Phys. Rev. Lett.

[115] T. Belgya, presentation at the 2015 Oslo Workshop.

[116] M. Guttormsen, T. Ramsøy, J. Rekstad, Nucl. Inst. Meth. A, **255**, 518 (1987).

[117] A. Schiller, L. Bergholt, M. Guttormsen, E. Melby, J. Rekstad, and S. Siem, Nucl. Instrum. Methods Phys. Res. A **447**, 498 (2000).

[118] E. Fermi, *Nuclear Physics*, University of Chicago Press, Chicago (1950).

[119] D. M. Brink, Nucl. Phys. **4**, 215 (1957).

[120] C. E. Porter and R. G. Thomas, Phys. Rev. **104**, 483 (1956).

[121] M. Guttormsen *et al.*, accepted for publication in EPJ A (2015).

[122] A. Voinov, M. Guttormsen, E. Melby, J. Rekstad, A. Schiller, and S. Siem, Phys. Rev. C **63**, 044313 (2001).

[123] H. Utsunomiya, A. Makinaga, S. Goko, T. Kaihori, H. Akimune, T. Yamagata, M. Ohta, H. Toyokawa, S. Müller, Y.-W. Lui, and S. Goriely, Phys. Rev. C **74**, 025806 (2006).

[124] H. Utsunomiya *et al.*, Phys. Rev. C **88**, 015805 (2013).

[125] M. Wiedeking, Private communication, Spring 2015.

[126] R. Schwengner, Private communication, Spring 2015.

[127] E. Mané, B. Cheal *et al.*, Phys. Rev. C **84**, 024303 (2011).

[128] A. Tonchev, presentation at the 2015 Oslo Workshop.

[129] Discussion session at the 2015 Oslo Workshop with George Bertsch, Yoram Alhassid, Vladimir Zelevinsky and others.

[130] S. Frauendorf, Rev. Mod. Phys. **73**, 463 (2001).

[131] T. Renstrøm *et al.*, to be submitted to Phys. Rev. C.

[132] A. Machiavelli *et al.*, GRETINA campaign in June 2015 @ ANL, ^{56}Fe (p, p$'$) @ E_p = 16 MeV (same reaction as A. C. Larsen *et al.*, Phys. Rev. Lett. **111**, 242504 (2013).

[133] Experiment IS559, Spokespersons S. Siem, and M. Wiedeking, see `https://cds.cern.ch/record/1482701?ln=en`.

[134] K. Yokoi, K. Takahashi, M. Arnould, Astronomy and Astrophysics **145**, 339 (1985).

[135] N. Mowlavi, S. Goriely, M. Arnould, Astronomy and Astrophysics **330**, 206 (1995).

[136] The homepage of HIγS,
`http://www.tunl.duke.edu/higs/layout/`.